



# High-performance double “ion-buffering reservoirs” of asymmetric supercapacitors enabled by battery-type hierarchical porous sandwich-like $\text{Co}_3\text{O}_4$ and 3D graphene aerogels

Changwei Lai<sup>1,2,3</sup> · Yao Guo<sup>1</sup> · Huihui Zhao<sup>1</sup> · Haixiang Song<sup>1</sup> · Xiaoxiao Qu<sup>3</sup> · Mina Huang<sup>5,6</sup> · Suck Won Hong<sup>3,4</sup> · Kwan Lee<sup>2</sup>

Received: 19 April 2022 / Revised: 22 May 2022 / Accepted: 29 June 2022 / Published online: 20 July 2022  
© The Author(s), under exclusive licence to Springer Nature Switzerland AG 2022

## Abstract

The double ion-buffering reservoirs of asymmetric supercapacitors (ASC) have drawn enormous interest due to their excellent electrochemical performance. Herein, we have prepared the hierarchical porous sandwich-like  $\text{Co}_3\text{O}_4$ -rGO-CNT > N-PEGm ( $\text{Co}_3\text{O}_4$ -RGOC, in which rGO was short for reduced graphene oxide and CNT > N-PEGm was modified with methoxypolyethylene glycol by nitrene chemistry) ternary composites via a solvothermal method. Remarkably, the  $\text{Co}_3\text{O}_4$ -RGOC composites exhibited unique structural features of the opened honeycomb-like structures as “ion-buffering reservoirs.” Moreover, in  $\text{Co}_3\text{O}_4$ -RGOC composites, both the intermediate sandwich layers of rGO sheets and the interpenetrating CNT > N-PEGms can form double conductive networks as express electron transport channels to improve the electronic conductivity by synergistic effect. The promising  $\text{Co}_3\text{O}_4$ -RGOC composites can be summarized as capacity of  $138.5 \text{ mAh g}^{-1}$  (capacitance of  $1420.5 \text{ F g}^{-1}$ ) at  $0.5 \text{ A g}^{-1}$ . Furthermore, the 3D rGO-PANI (PANI, polyaniline) aerogels as negative electrode materials also have been prepared by facile in situ polymerization and chemical reduction process. The 3D rGO-PANI presented excellent electrochemical performance of  $218.8 \text{ F g}^{-1}$  (capacity of  $60.8 \text{ mAh g}^{-1}$ ) at  $0.5 \text{ A g}^{-1}$  due to the hierarchical interconnected porous network structures. Finally, the corresponding asymmetric supercapacitors of  $\text{Co}_3\text{O}_4$ -RGOC//3D rGO-PANI devices exhibited a high energy density of  $41.3 \text{ Wh kg}^{-1}$  at power densities of  $775 \text{ Wk g}^{-1}$  with excellent electrochemical performance and long cycle performance. Our work can present a new concept to design the innovative asymmetric supercapacitors with double ion-buffering reservoirs as a combinatorial strategy for useful energy storage and conversion.

**Keywords** Ion-buffering reservoir ·  $\text{Co}_3\text{O}_4$  · Double conductive networks · Graphene aerogels · Asymmetric supercapacitor

✉ Changwei Lai  
laichangwei0229@163.com

✉ Haixiang Song  
13837213690@163.com

✉ Suck Won Hong  
swhong@pusan.ac.kr

✉ Kwan Lee  
kwanlee@ks.ac.kr

<sup>1</sup> Henan Joint International Research Laboratory of Nanocomposite Sensing Materials, School of Materials Science and Engineering, Anyang Institute of Technology, Anyang 455000, People's Republic of China

<sup>2</sup> Department of Advanced Materials Engineering, Kyungsoong University, Busan 48434, Republic of Korea

<sup>3</sup> Department of Cogno-Mechatronics Engineering, College of Nanoscience and Nanotechnology, Pusan National University, Busan 46241, Republic of Korea

<sup>4</sup> Department of Optics and Mechatronics Engineering, College of Nanoscience and Nanotechnology, Pusan National University, Busan 46241, Republic of Korea

<sup>5</sup> College of Materials Science and Engineering, Taiyuan University of Science and Technology, Taiyuan 030024, People's Republic of China

<sup>6</sup> Integrated Composites Laboratory (ICL), Department of Chemical and Biomolecular Engineering, University of Tennessee, Knoxville, TN 37996, USA

## 1 Introduction

Owing to the global energy crisis and environmental protection requirements, the new generation of clean and low cost energy resources has been urgent demand in the energy storage-conversion field, such as supercapacitors [1–7], lithium-ion batteries [8–10], lithium–oxygen batteries [11], and other aqueous rechargeable batteries [12]. Among other developing alternative energy storage devices, the asymmetric supercapacitors (ASC) of double *ion-buffering reservoirs* have attracted significant attention because of their better safety, quick charge/discharge ability, and ultra-long cycling performance, and high energy/power density [13–17]. Recently, the asymmetric supercapacitors, built with double “ion-buffering reservoirs,” have been designed by the metal oxides/hydroxide and carbon aerogels both with the hierarchical opened honeycomb-like porous structures to boost the electrochemical performance. In this ASC structure, the typical electrode materials are composed of ultrathin paper-like nanosheets with interconnected porous networks and opened hierarchically honeycomb-like structures, which are fully utilized as ion-buffering reservoirs [18, 19]. During the typical electrochemical charge–discharge process, the electrolyte ions can be filled in the structured ion-buffering reservoirs and easily transported into the interior surfaces of the electrode materials with a shortened diffusion distance to ensure sufficiently reversible redox reaction even at high current densities (or high scan rates) [20]. Meanwhile, to obtain a wider operating voltage window, the ASC devices can be assembled with both the battery-type positive electrode materials as energy sources associated with reversible Faradaic redox reactions and the negative electrode materials as power sources based on surface/near-surface capacitive behaviors in a single device to further enhance the energy density [21–23]. Among the transition metal oxide (TMOs) [24–28], the typical battery-type electrode materials of  $\text{Co}_3\text{O}_4$  have stimulated extensive interest due to high natural abundance, low cost, environmental friendliness, theoretical capacitance ( $3560 \text{ F g}^{-1}$ ), and high electrochemical performance [29–31]. Especially, the hierarchical porous  $\text{Co}_3\text{O}_4$  structures have exhibited remarkable characteristics of interconnected porous networks, short ion diffusion channels, and enlarged surface area to ensure high electrochemical performance [32, 33]. However, the  $\text{Co}_3\text{O}_4$  also suffers from low electric conductivity and limited capacitance. Interestingly, two elegant strategies, both surface areas and doping carbon materials, can be employed to enhance the electrochemical performance by improving the reversible redox-active sites and electron transport [15], respectively. In this context, there remain challenges in designing new hierarchical porous sandwich-like structures of  $\text{Co}_3\text{O}_4$  composites for promising electrochemical performance.

Various types of carbon materials have been widely applied in many fields [34–36]. Recently, it has been demonstrated that graphene aerogels (GAs) [37–39] as electrical double-layer capacitors (EDLCs) [40, 41] exhibit interconnected porous networks with opened honeycomb-like porous structures as ion-buffering reservoirs [13–15]. In this structured arrangement, the walls of porous graphene networks can be filled with the substantial electrolyte ions in graphene pore walls during the charge–discharge processes, which are composed of randomly oriented and crinkly graphene nanosheets. However, the GAs still suffer from the restacking and agglomeration in the 3D foam-structured process due to the van der Waals forces and  $\pi$ – $\pi$  stacking interaction, thus triggering the deteriorated surface and decreased specific capacitance [42]. On the other hand, the conductive polymers (e.g., PANI) present low cost, environmental friendliness, reversible redox reaction, and excellent chemical stability [43, 44]. Hence, by introducing PANI, the graphene-PANI composites can achieve a large surface area, hydrophilicity, extraordinary mechanical, and excellent electronic conductivity [45]. Accordingly, the advanced rGO-PANI composites can be prepared as hopeful EDLC electrode materials.

Herein, we developed the hierarchically porous sandwich-like  $\text{Co}_3\text{O}_4$ -RGOC ternary composites with ultrathin nanosheets by a solvothermal method, in which the interpenetrating rGO and CNTs can act as double conductive networks in the interior; meanwhile, the opened honeycomb-like structures as typical “ion-buffering reservoirs” can be filled with electrolyte on the exterior. Simultaneously, the promising 3D rGO-PANI aerogels have been prepared via facile in situ polymerization and hydrothermal reduction. Additionally, the typical novel asymmetric supercapacitor  $\text{Co}_3\text{O}_4$ -RGOC//3D rGO-PANI with double ion-buffering reservoirs present excellent electrochemical properties with specific capacitance, high rate performance, and long cycle life.

## 2 Experimental

### 2.1 Materials

All reagents used in this work are analytical grade.  $\text{Co}(\text{NO}_3)_2 \cdot 6\text{H}_2\text{O}$  (>98.5%), methanol (>99.7%), N-methyl-2-pyrrolidone (NMP, 99.5%), acetylene black, polyvinylidene difluoride (PVDF), poly(vinyl alcohol) 1799 (PVA) (>98.0%), and KOH (>85.0%) were purchased from Sinopharm Chemical Reagent Co., Ltd. And aniline (99.5%), ammonium persulfate (APS, 98%), L-ascorbic acid (99%), and methoxypolyethylene glycol (mPEG, Mw=5000) were bought from Aladdin Chemical Reagent Co., Ltd. The flake graphite and CNT were purchased from Nanjing/Jiangsu XFNANO Materials Tech Co., Ltd. The graphene oxides (GO) were synthesized by a modified Hummers’ method [15].

## 2.2 Synthesis of Co<sub>3</sub>O<sub>4</sub>-RGOC ternary composites

The Co<sub>3</sub>O<sub>4</sub>-RGOC composites were synthesized with 1.5 g of Co(NO<sub>3</sub>)<sub>2</sub>·6H<sub>2</sub>O and 100 mg of GO/CNT>N-PEGm powder as previously reported [13, 14], in which the GO/CNT>N-PEGm (RGO/C) were prepared with different mass ratio of 4:1, 2:1, 1:1, 1:2, and 1:4 (denoted as Co<sub>3</sub>O<sub>4</sub>-RGOC-(4–1), Co<sub>3</sub>O<sub>4</sub>-RGOC-(2–1), Co<sub>3</sub>O<sub>4</sub>-RGOC-(1–1), Co<sub>3</sub>O<sub>4</sub>-RGOC-(1–2), Co<sub>3</sub>O<sub>4</sub>-RGOC-(1–4)), respectively.

## 2.3 Synthesis of 3D rGO-PANI

The 3D rGO-PANI aerogels were prepared as previously reported [16, 17] by two steps: polymerization and hydrothermal reduction. The GO aqueous dispersion (50 mL, 2 mg mL<sup>-1</sup>), 1 M HCl (50 mL), and aniline monomer (25 mg) were mixed uniformly and sonicated for 0.5 h. Subsequently, the initiator of ammonium persulfate (APS, 0.5 mg) dissolved in water (20 mL) was added by dropwise. After polymerization for 10 h, the GO-PANI composites were reduced with L-ascorbic acid (80 mg) at 120 °C for 4 h by hydrothermal method. Finally, the as-prepared rGO-PANI were soaked and dried by freeze-drying to form 3D rGO-PANI aerogels.

## 2.4 Characterizations

The as-prepared Co(OH)<sub>2</sub>-RGOC precursors, Co<sub>3</sub>O<sub>4</sub>-RGOC composites, and 3D rGO-PANI aerogels were characterized by Raman spectroscopy (Labram HR800 Raman Microprobe), transmission electron microscopy (TEM, Philips Tecnai-12), TGA (SDT-Q600), X-ray diffraction (XRD) (Bruker, D8-Discover Germany), X-ray photoelectron spectroscopy (XPS) spectra (ESCALAB-250), scanning electron microscopy (SEM, HITACHI S-4800), and the nitrogen adsorption/desorption isotherms (3H-2000PS1) with Brunauer – Emmert – Teller (BET) and Barrett – Joyner – Halenda (BJH) methods, respectively.

## 2.5 Electrochemical characterization

The electrode materials of both Co<sub>3</sub>O<sub>4</sub>-RGOC composites and 3D rGO-PANI aerogels were systematically evaluated in three-electrode configuration such as cyclic voltammograms (CV), galvanostatic charge–discharge (GCD), and electrochemical impedance spectroscopy (EIS) measurements in 6 M KOH aqueous solution with reference electrode of Ag/AgCl and electrochemical workstation (CHI660E). The specific capacities and capacitance were calculated by the following equation:

$$C^* = \frac{It}{3.6m} \text{ and } C = \frac{It}{mV} \quad (1)$$

wherein  $C^*$ ,  $C$ ,  $I$ ,  $t$ ,  $V$ , and  $m$  were the specific capacity (mAh g<sup>-1</sup>), capacitance (F g<sup>-1</sup>), discharge current (A), discharging time (s), discharge voltage window (V), and the load mass of actives materials on the electrode (g), respectively. Similarly, in the two-electrode system (in 6 M KOH), the Co<sub>3</sub>O<sub>4</sub>-RGOC//3D rGO-PANI asymmetric supercapacitor devices were assembled with Co<sub>3</sub>O<sub>4</sub>-RGOC (0.8 mg) and 3D rGO-PANI (1.8 mg). Owing to charge balanced equation ( $Q_+ = Q_-$ ), the optimal electrode mass ratio positive/negative (as  $m_+ / m_-$ ) was calculated as the following equation:

$$\frac{m_+}{m_-} = \frac{C_- \cdot \Delta V_-}{C_+ \cdot \Delta V_+} \quad (2)$$

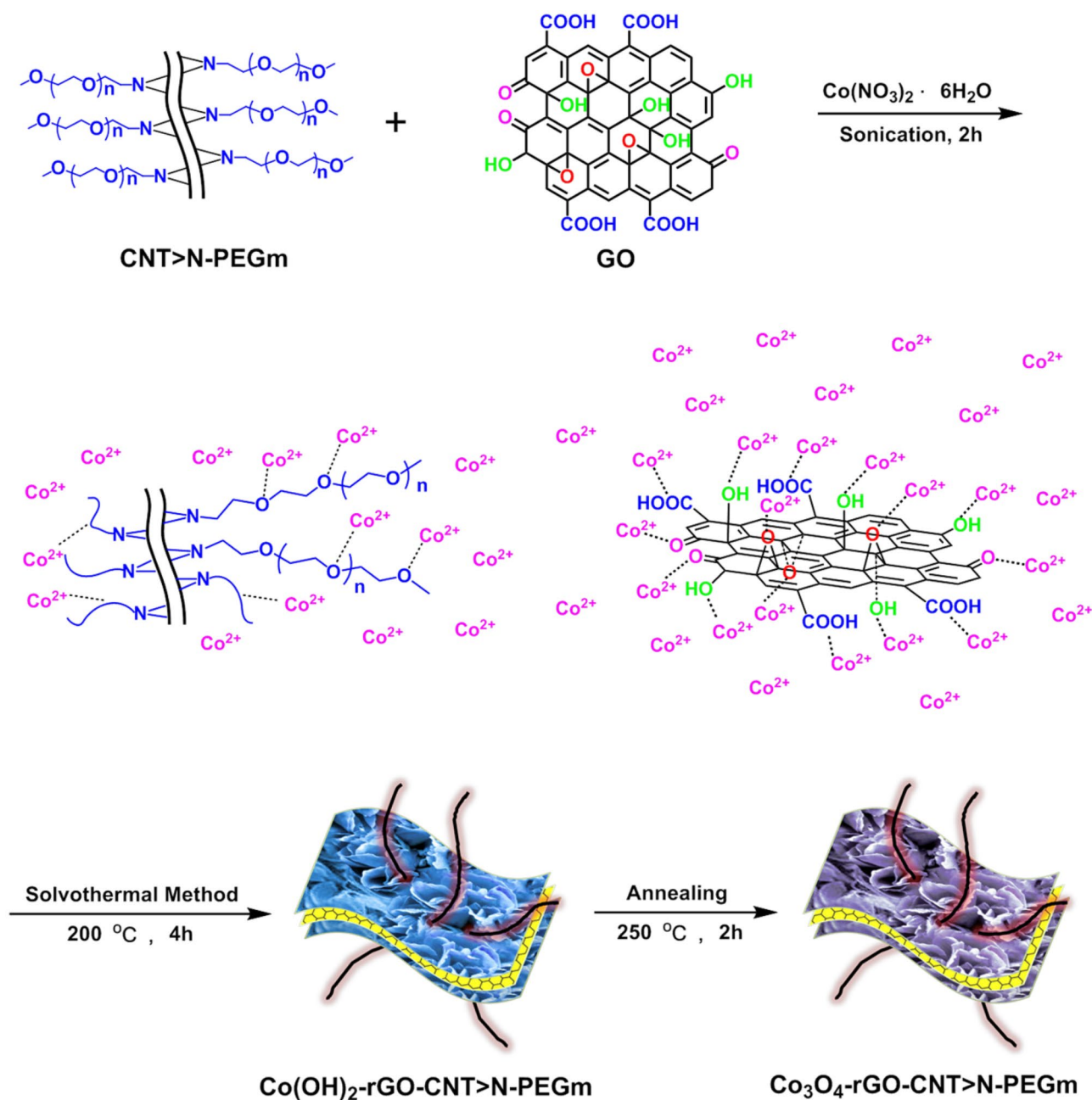
The power density ( $P$ , W kg<sup>-1</sup>) of the obtained device and energy density ( $E$ , Wh kg<sup>-1</sup>) were calculated by following equations:

$$E = \frac{C \cdot (\Delta V)^2}{2 \times 3600} \quad (3)$$

$$P = \frac{3600 \cdot E}{\Delta t} \quad (4)$$

## 3 Results and discussion

The synthetic procedure of the hierarchical porous sandwich-like Co<sub>3</sub>O<sub>4</sub>-rGO-CNT>N-PEGm (Co<sub>3</sub>O<sub>4</sub>-RGOC) ternary composites has been presented in Scheme 1. In this typical preparation process, the carbon materials, such as graphene oxide (GO) and CNT>N-PEGm (modified with the methoxypolyethylene glycol (mPEG) by nitrene chemistry, in which “>” represents the aziridine ring) [18], were introduced via a facile solvothermal method to obtain the Co(OH)<sub>2</sub>-rGO-CNT>N-PEGm (Co(OH)<sub>2</sub>-RGOC) composites as precursors. Subsequently, the precursors can be further sintered to give rise to the sandwich-like Co<sub>3</sub>O<sub>4</sub>-RGOC ternary composites with the keeping morphology and structures of double conductive networks. Notably, the precursors of Co(OH)<sub>2</sub>-RGOC composites exhibited hierarchical porous sandwich-like structure surface morphology (Fig. 1a–c). A part of the CNT>N-PEGms anchored on the 2D surface of heavily reduced graphene oxide (rGO) sheets (i.e., intermediate sandwich layers) to effectively prevent the GO sheets from restacking during the building process of sandwich-like structures (Fig. 1c, e). On the other hand, the other part also can be uniformly inserted into the hierarchical porous opened honeycomb-like structures to form the interpenetrating rGO/CNTs networks as the express electron transport channels. Remarkably, the ultrathin nanosheets of Co(OH)<sub>2</sub> only present 2–4 nm (Fig. 1d), indicating



**Scheme 1** Schematic illustration of the preparation processes of the hierarchical porous sandwich-like Co<sub>3</sub>O<sub>4</sub>-rGO-CNT>N-PEGm ternary composites

the specific surface area of 134.14 m<sup>2</sup> g<sup>-1</sup>, in which the BJH pore size distribution was found to be ~ 3.9 nm. Here, the lattice space of 0.34 nm might be attributed to the (002) planes of CNTs as appeared in the HRTEM images (Fig. 1f).

In the typical solvothermal preparation, the  $\alpha$ -type polymorph (i.e., hydroxalcite-like structure) of the Co(OH)<sub>2</sub>-RGOC was produced with dodecylbenzene sulfate (DBS)-intercalated structures in the (003) plane as shown in Fig. 2a. This result

can be further determined S element at the peak of 2.3 keV in the EDS spectrum (Fig. 2b) [46]. Besides, in Fig. 2i, the EDS elemental mapping analysis further demonstrates the typical DBS-intercalated structures, where a series of elements Co, O, C, S, and Cl are distributed uniformly in the hierarchical porous sandwich-like structures, as presented in Fig. 2c-j. These results imply that the expected sandwich-like structures with ultrathin nanosheets are successfully synthesized by our optimized solvothermal process.

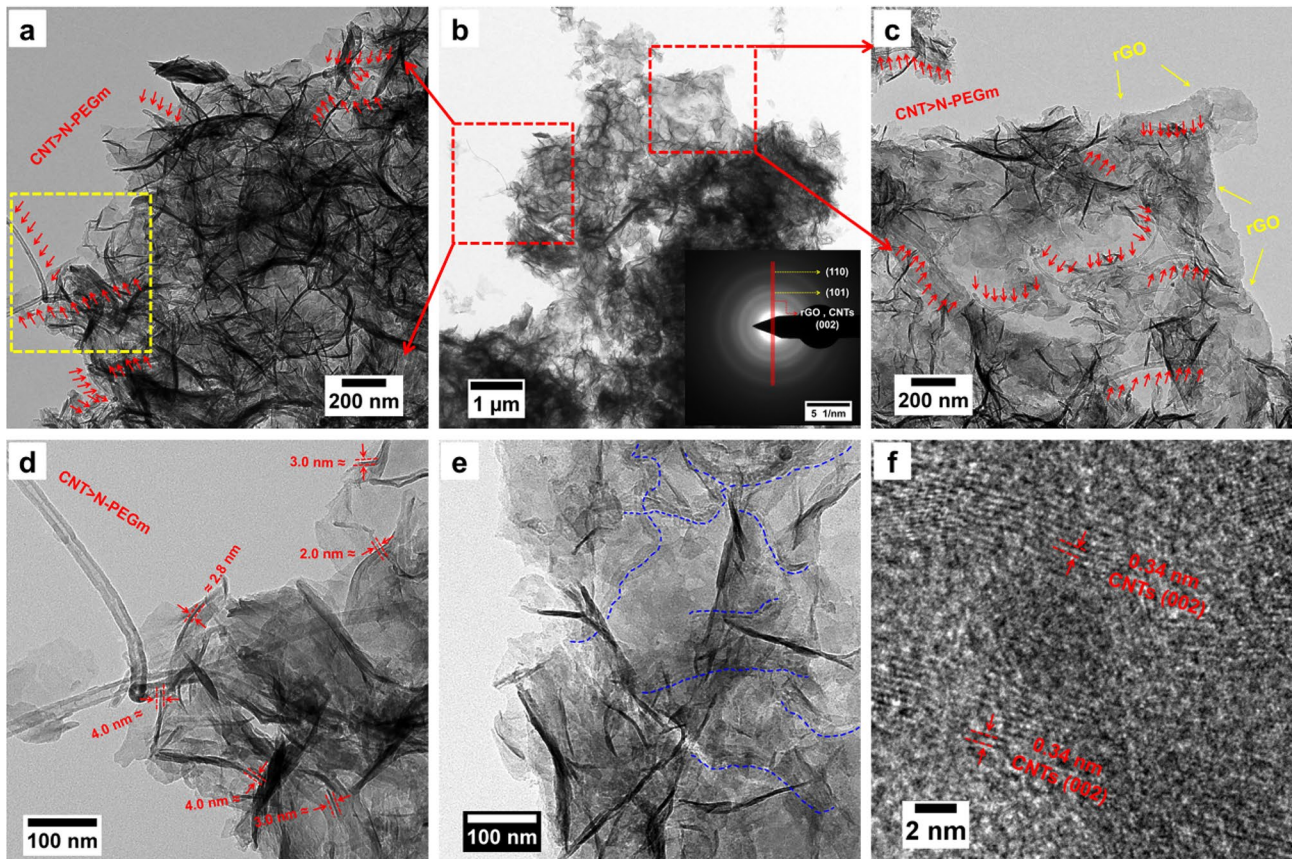


**Fig. 1** a–e Low- and high-magnification TEM images and SAED pattern (inset), and **f** HRTEM images of  $\text{Co}(\text{OH})_2$ -RGOC ternary composites

In Fig. 3a, the TGA–DSC curves of  $\text{Co}(\text{OH})_2$ -RGOC composites were carried out (in air) to further confirm the chemical composition (Fig. S1 and Table S1), according to seven stages as (S-I) evaporation of the adsorbed surface water, (S-II) removal of the intercalated water in (003) plane, (S-III) thermal oxidative decomposition of  $\text{Co}(\text{OH})_2$  to  $\text{Co}_3\text{O}_4$  at  $\sim 273$  °C and the side chains mPEG of CNT > N-PEGm both with weight loss of 22.2%, (S-IV) combustion of other organic matter and part carbon atoms by oxygen etching, (S-V) thermal oxidation of  $\text{DBS}^-$  ions, (S-VI) combustion of the incorporating graphene nanosheets and CNTs at around 548 °C, and (S-VII) oxidation of  $\text{CoSO}_4$  to  $\text{Co}_3\text{O}_4$  at around 726 °C (according to the transformation of  $\text{CoSO}_4$  into  $\text{Co}_3\text{O}_4$ ) [15], respectively. Directly compared to the  $\alpha$ -type polymorph of  $\text{Co}(\text{OH})_2$ -RGOC (JCPDS 51–1731, the (003) planes of  $\text{Co}(\text{OH})_2$  moved to  $2\theta = 11.6^\circ$  due to the typical  $\text{DBS}^-$ -intercalated structures), the  $\text{Co}_3\text{O}_4$ -RGOC ternary composites were evidenced in the cubic phase based on the (111), (220), (311), (222), (400), (422), (511), and (440) planes (JCPDS 42–1467), as shown in the XRD patterns (Fig. 3b). The peak at  $2\theta = 25.8^\circ$  is attributed to both the (002) planes of CNTs and rGO nanosheets. Moreover, the Raman spectroscopy was used

to evaluate the essential components of  $\text{Co}_3\text{O}_4$ -RGOC (Fig. 3c), which displayed the peaks at 185 ( $F_{2g}$ ), 463 ( $E_g$ ), 511 ( $F_{2g}$ ), and 670 ( $A_{1g}$ )  $\text{cm}^{-1}$ , corresponding to the  $\text{Co}_3\text{O}_4$  features. Furthermore, the CNTs and rGO nanosheets were found separately in the peaks at 1345 (D), 1576 (G), and 2689 (2D)  $\text{cm}^{-1}$  [18, 19], respectively.

For more detailed chemical information, the XPS measurement displays the as-synthesized samples  $\text{Co}(\text{OH})_2$ -RGOC,  $\text{Co}_3\text{O}_4$ -RGOC-250, and  $\text{Co}_3\text{O}_4$ -RGOC-350 (sintering at 250 and 350 °C) in Fig. 3d–f. Importantly, the XPS analysis further verified the coordination bonds in the  $\text{Co}_3\text{O}_4$ -RGOC ternary composites between the ether–oxygen groups of CNT > N-PEGms and cobalt ions (Fig. S2). As presented in Fig. 3d, the high-resolution Co 2p spectroscopy of  $\text{Co}(\text{OH})_2$ -RGOC displays two peaks of 782.3 (Co 2p<sub>3/2</sub>) and 798.3 eV (2p<sub>1/2</sub>) with 787.1 and 804.3 eV as two shake-up satellite peaks (denoted as “Sat.”), thus suggesting the  $\text{Co}(\text{OH})_2$  formation with spin–orbit splitting of 16.0 eV [47], respectively. Moreover, the Co 2p spectrum of  $\text{Co}_3\text{O}_4$ -RGOC-250 and  $\text{Co}_3\text{O}_4$ -RGOC-350 exhibited the Co 2p<sub>3/2</sub> (at 781.3 eV) and Co 2p<sub>1/2</sub> (at 796.3 eV) peaks, which can be fitted to  $\text{Co}^{2+}$  (at 782.4 and 798.1 eV) and  $\text{Co}^{3+}$  (at 781.1 and 796.2 eV) [48, 49], respectively. To verify the formation of coordination bonds, we also surveyed the O

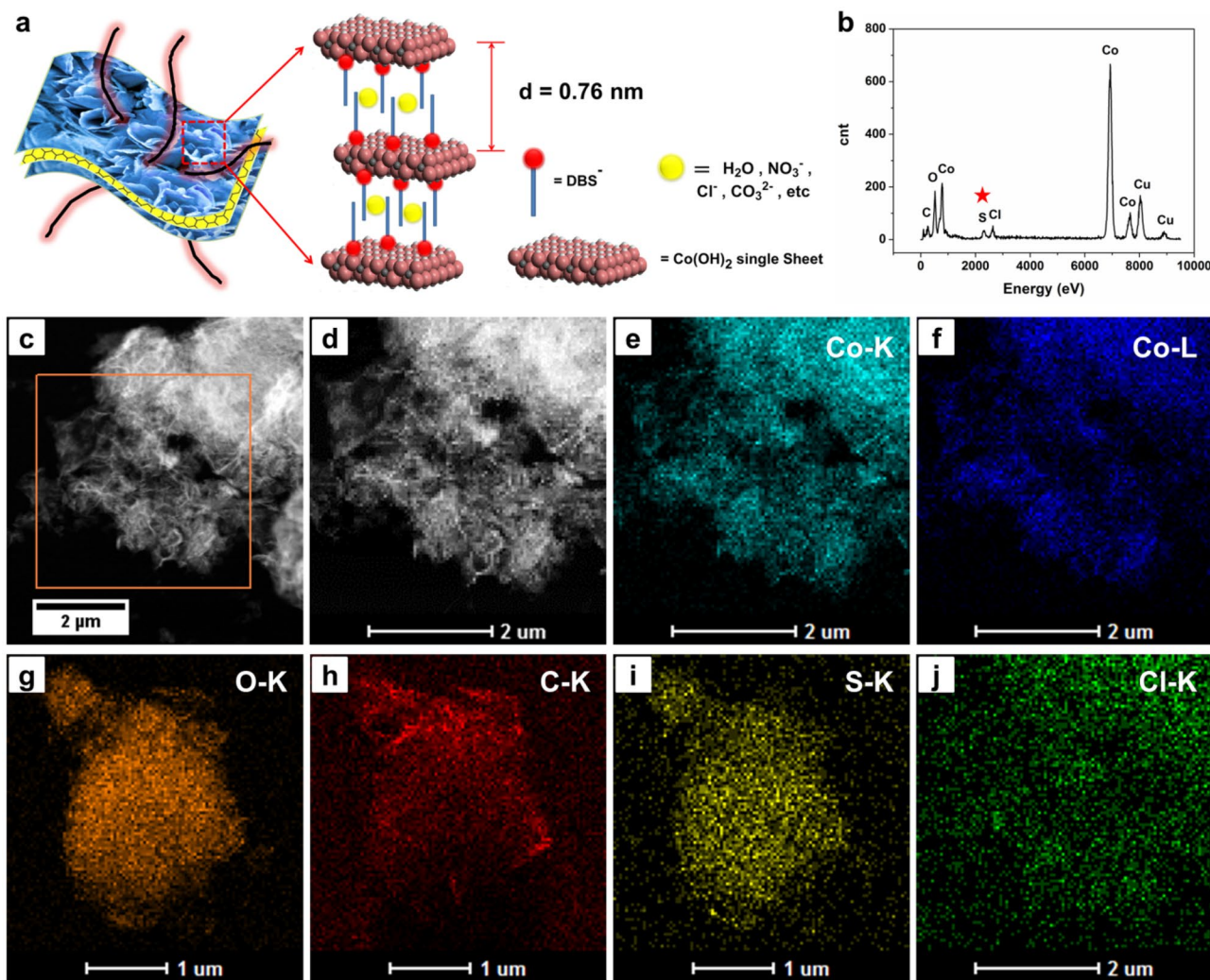


**Fig. 2** a Schematic illustration of the DBS-intercalated  $\text{Co(OH)}_2$ -RGOC composites. b EDS spectrum, c STEM image, and d–j the EDS elemental mapping analysis of Co-K, Co-L, O-K, C-K, S-K, and Cl-K of  $\text{Co(OH)}_2$ -RGOC

1 s spectra (Fig. 3e) of  $\text{Co(OH)}_2$ -RGOC,  $\text{Co}_3\text{O}_4$ -RGOC-250, and  $\text{Co}_3\text{O}_4$ -RGOC-350 composites. The O 1 s spectra of  $\text{Co(OH)}_2$ -RGOC can be represented by two mainly deconvoluted peaks at 531.4 eV (Co–OH) and 532.6 eV (S–O, as intercalated  $\text{DBS}^-$  ions), respectively. During the annealing process, the transformations of  $\text{Co(OH)}_2$  to  $\text{Co}_3\text{O}_4$ , the O 1 s spectra of  $\text{Co}_3\text{O}_4$ -RGOC-250 and  $\text{Co}_3\text{O}_4$ -RGOC-350 can be attributed to the lattice oxide ions “ $\text{O}^{2-}$ ” (530.3 eV), defective oxide ions “ $\text{O}^{x-}$ ” (531.8 eV), S–O (532.6 eV as doping  $\text{DBS}^-$  ions), C–O–C (533.2 eV), and  $\text{H}_2\text{O}$  (534.2 eV, the surface adsorbed water) [18, 19], respectively. It is worth to note that the peak at 531.2 eV for  $\text{Co}_3\text{O}_4$ -RGOC-250 can be obviously assigned to the coordination bonds of  $\text{Co} \leftarrow \text{O} - \text{C}$ , indicating that the defective oxide “ $\text{O}^y-$ ” ions under-coordinated (as  $\text{C} - \text{O} \rightarrow \text{Co} - \text{O}^y-$ ) bear higher electron density than the bare defective oxide “ $\text{O}^x-$ ” ions (as  $\text{Co} - \text{O}^x-$ ) ( $y > x$ ) [18, 19]. Further, to confirm the coordination bonds, the defective

oxygen peak of  $\text{Co}_3\text{O}_4$ -RGOC-350 occurs at 531.8 eV, while that of  $\text{Co}_3\text{O}_4$ -RGOC-250 occurs at 531.6 eV (at lower binding energy), thus differing by 0.2 eV for the relevant band positions due to the coordination effect. In addition, the S 2p XPS spectra in Fig. 3f for  $\text{Co(OH)}_2$ -RGOC,  $\text{Co}_3\text{O}_4$ -RGOC-250, and  $\text{Co}_3\text{O}_4$ -RGOC-350 displayed the peaks at 168.5 eV (sulfate to  $\text{Co}^{2+}$  in tetrahedral sites) and 169.6 eV (sulfate to  $\text{Co}^{3+}$  in octahedral sites), indicating that the sulfate to  $\text{Co}^{3+}$  bears lower electron density due to the polarization by electron-withdrawing from S to O) [13]. Hence, the XPS analysis clearly confirmed the DBS-intercalated structure of  $\text{Co(OH)}_2$ -RGOC precursors and the  $\text{DBS}^-$  ion-doped structure of  $\text{Co}_3\text{O}_4$ -RGOC composites.

The surface morphologies of the hierarchical porous sandwich-like  $\text{Co}_3\text{O}_4$ -RGOC were observed by SEM (Fig. 4a, b). From this measurement, we found that the opened honeycomb-like hierarchically porous structures

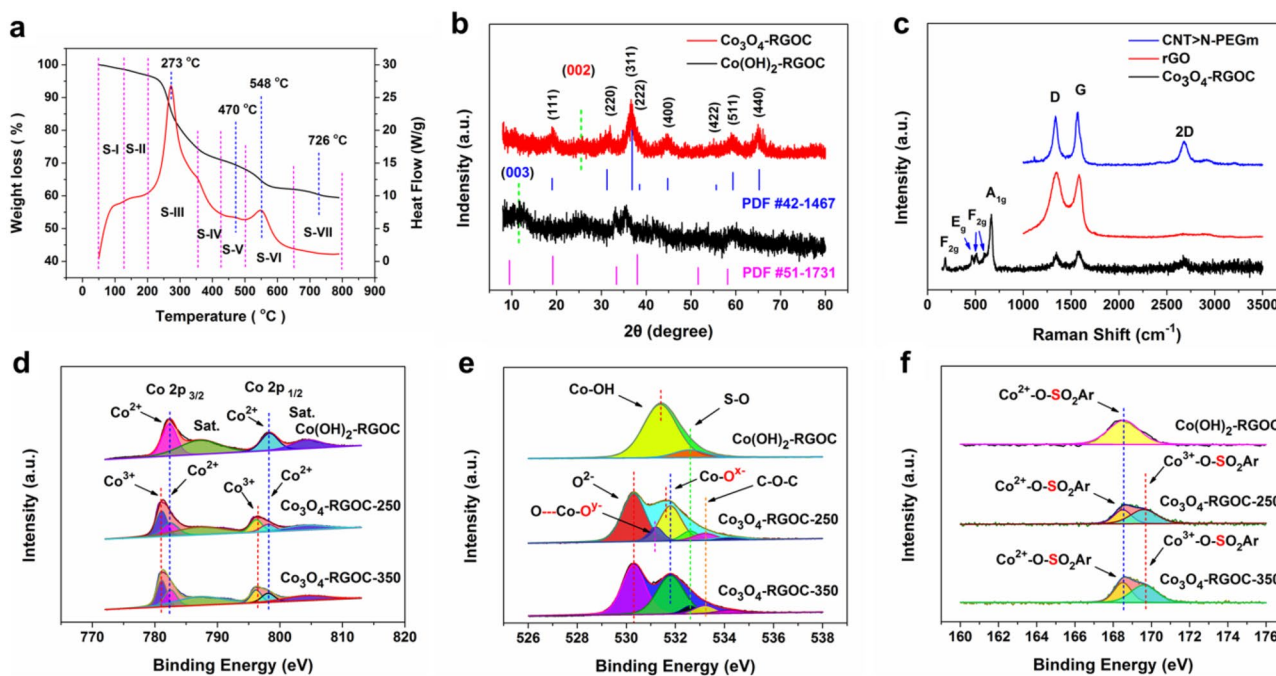


**Fig. 3** **a** TGA–DSC curve of  $\text{Co}(\text{OH})_2$ -RGOC in air. **b** XRD patterns of  $\text{Co}(\text{OH})_2$ -RGOC and  $\text{Co}_3\text{O}_4$ -RGOC composites. **c** Raman spectra of CNT>N-PEGm, rGO, and  $\text{Co}_3\text{O}_4$ -RGOC composites. The XPS

characterization of  $\text{Co}(\text{OH})_2$ -RGOC and  $\text{Co}_3\text{O}_4$ -RGOC (sintering at 250 and 350 °C) composites: **d** Co 2p, **e** O 1s, and **f** S 2p spectra

are composed of the randomly and crinkly ultrathin  $\text{Co}_3\text{O}_4$  nanosheets as pore walls to form the *ion-buffering reservoir* structures, which can be filled with aqueous electrolyte solution in the interconnected network spaces to reduce the contact resistance between the electrolyte and  $\text{Co}_3\text{O}_4$ -RGOC composites at the interface (Fig. S3). Moreover, the intermediate sandwich layers of rGO sheets and the interpenetrating CNT>N-PEGms were formed as double conductive networks for express electron transport channels, which are highly beneficial for the electron transport by synergistic effect in sandwich-like  $\text{Co}_3\text{O}_4$ -RGOC ternary composites. In addition, as shown in Fig. 4c–h, the elements (i.e., Co, O, C, S, and Cl) are distributed uniformly in  $\text{Co}_3\text{O}_4$ -RGOC composites, indicating that the DBS-intercalated structures in  $\alpha$ -type polymorph  $\text{Co}(\text{OH})_2$  translate into the  $\text{DBS}^-$  ion-doped structures in the cobalt spinel oxide (Fig. S4).

As presented in Fig. 5a–e, the hierarchical porous sandwich-like structures of  $\text{Co}_3\text{O}_4$ -RGOC composites were revealed by the TEM measurement (Fig. S5), representing the results of the interlinked and intercrossed rGO/CNTs by the formation of the double conductive networks (Fig. S6). More interestingly, ultrathin  $\text{Co}_3\text{O}_4$  nanosheets (i.e., ~2–4 nm) exhibited abundant hierarchical mesoporous structures by the *Kirkendall* effect [50, 51]; these are beneficial for electrolyte ions due to the short ion diffusion channels in the charge–discharge process. Moreover, the HRTEM

image (Fig. 5f) displays the lattice spacings of 0.34, 0.46, and 0.28 nm, corresponding to the (002) planes of CNTs, (111), and (220) planes in the cubic  $\text{Co}_3\text{O}_4$  crystal structure. In addition, the SAED patterns (inset) represented a polycrystalline feature of the  $\text{Co}_3\text{O}_4$  particles by the primary rings. Compared to the previously reported  $\text{Co}_3\text{O}_4$ -based electrode materials, the  $\text{Co}_3\text{O}_4$ -RGOC composites with abundant mesoporous scale pores represent the Langmuir type IV (Fig. S7 and Table S2) [11, 52], the BET surface area of  $167.99 \text{ m}^2 \text{ g}^{-1}$ , the BJH pore size distribution range of 1.9–3.7 and 13–30 nm, and pore volume of  $1.07 \text{ mL g}^{-1}$ , respectively. Based on the excellent attributes of the typical structures, several advantageous outcomes can be summarized as follows: (i) the specific surface area provides abundant reversible Faradaic redox sites; (ii) the interconnected porous hierarchically opened honeycomb-like structures can ensure the external electrolyte ions complete infiltration; (iii) the numerous nanoscale pores in the  $\text{Co}_3\text{O}_4$  nanosheets can further confirm the  $\text{OH}^-$  ions transporting with shortened ion diffusion channels; and (iv) a series of CNTs and intermediate sandwich rGO sheets may act as “express channels” to improve the electronic conductivity and electrochemical stability. Consequently, the battery-type  $\text{Co}_3\text{O}_4$ -RGOC composites can be deemed as promising rechargeable electrode materials for excellent electrochemical performance.

The electrochemical properties of  $\text{Co}_3\text{O}_4$ -RGOC composites were systematically evaluated in a three-electrode

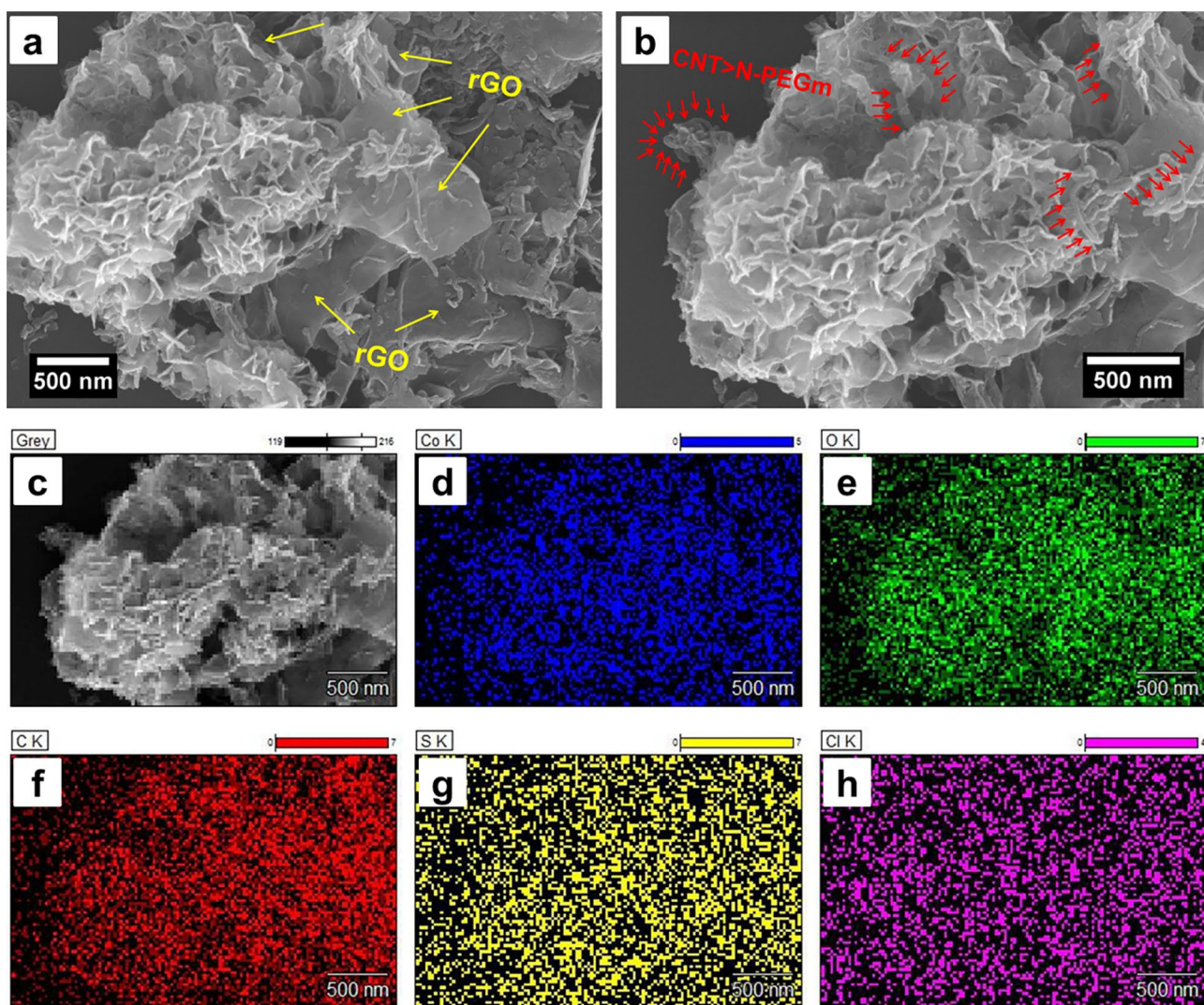
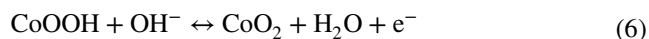


**Fig. 4** The SEM characterization of  $\text{Co}_3\text{O}_4$ -RGOC composites: **a** low- and **b** high-magnification SEM images, **c–h** the EDS elemental mapping analysis of Co-K, O-K, C-K, S-K, and Cl-K

configuration with 6 M KOH aqueous solution. Compared with  $\text{Co}(\text{OH})_2$ -RGOC and  $\text{Co}_3\text{O}_4$ -RGOC-350, the electrode materials of  $\text{Co}_3\text{O}_4$ -RGOC-250 showed a larger CV curve area at  $100 \text{ mV s}^{-1}$  and superior electrochemical performance in Fig. 6a. Moreover, from the GCD curves (Fig. 6b) at  $0.5 \text{ A g}^{-1}$ , it was found that  $\text{Co}_3\text{O}_4$ -RGOC-250 possesses a higher specific capacity. The graphs in Fig. 6c exhibit the average (at least four samples) specific capacity of  $\text{Co}(\text{OH})_2$ -RGOC,  $\text{Co}_3\text{O}_4$ -RGOC-250, and  $\text{Co}_3\text{O}_4$ -RGOC-350 at various current densities for comparison, and  $\text{Co}_3\text{O}_4$ -RGOC-250 reveals the highest capacity value of  $138.5 \text{ mAh g}^{-1}$  (corresponding to the capacitance of  $1420.5 \text{ F g}^{-1}$ ) at  $0.5 \text{ A g}^{-1}$  (Fig. S8). To further investigate the specific capacity value of  $\text{Co}_3\text{O}_4$ -RGOC-250 in Fig. 6d, the rGO/CNT mass ratio was adjusted as 4:1, 2:1, 1:1, 1:2, and 1:4, respectively. In an optimized condition, the  $\text{Co}_3\text{O}_4$ -RGOC-(4-1) markedly

represented superior capacity to other samples. Accordingly, the CV curves deliver good reversibility of the obvious reversible Faradaic redox reactions and fast charge–discharge response at various increased scan rates, ranging from 2 to  $100 \text{ mV s}^{-1}$ , as exhibited in Fig. 6e, exhibiting typical battery-type behavior based on the  $\text{Co}^{2+}/\text{Co}^{3+}/\text{Co}^{4+}$  at different cobalt oxidation states as follows [53]:



Owing to Dunn method [54], the charge storage kinetics were investigated by the  $\log(i)$  versus  $\log(v)$  as follows:

$$\log i = b \log v + \log a \quad (7)$$



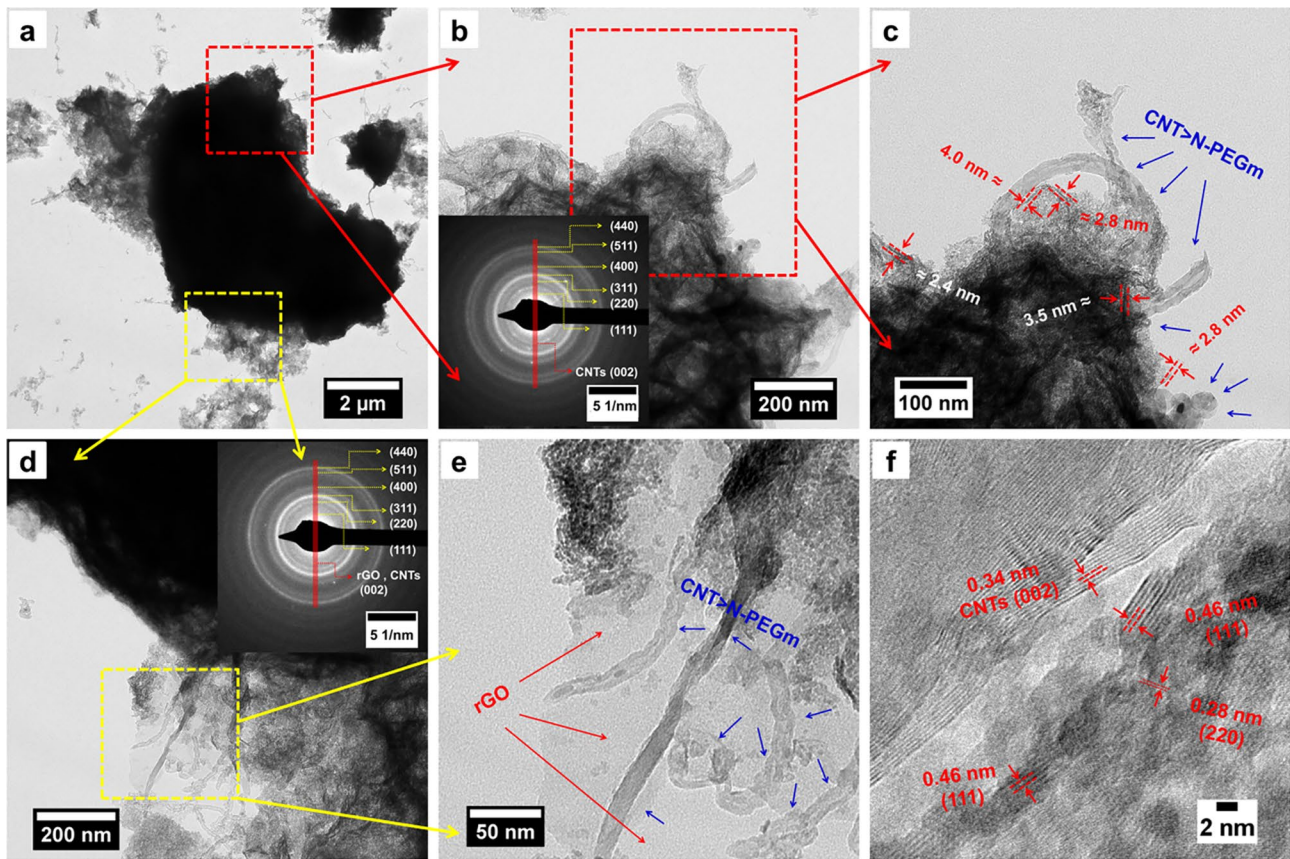


**Fig. 5** The TEM characterization of  $\text{Co}_3\text{O}_4$ -RGOC composites: **a–e** Low- and high-magnification TEM images and SAED pattern (inset), **f** HRTEM image

where  $a$  and  $b$  are adjustable parameters and so  $i$  current density ( $\text{A g}^{-1}$ ) and  $v$  scan rate ( $\text{mV s}^{-1}$ ), respectively. Remarkably, the  $b$  values can be determined as 0.746 and 0.833 (in range of 0.5–1.0) in Fig. 6f, indicating the pseudocapacitive- and battery-type characteristics simultaneously occurred in the  $\text{Co}_3\text{O}_4$ -RGOC electrodes (Fig. S9). Moreover, the capacitive and diffusion-controlled ratio can be confirmed by the surface capacitance-led ( $I_{\text{cap}}$ ) and diffusion-controlled ( $I_{\text{diff}}$ ) processes as the following equations [55, 56]:

$$I = I_{\text{cap}} + I_{\text{diff}} = av^b \quad (8)$$

Consequently, the capacitive-controlled processes are 54.4%, 62.2%, 67.3%, 72.1%, 75.1%, 79.7%, and 90.3% at various scan rates of 2, 5, 10, 20, 30, 50, and 100  $\text{mV s}^{-1}$ , respectively, as presented in Fig. 6g. Moreover, Fig. 6h shows the GCD curves with the voltage plateaus versus typical battery-type behavior at different current densities (0.5 to 40  $\text{A g}^{-1}$ ), corresponding to the obvious redox peaks in the CV curves (Fig. S10a). In Fig. 6i, the rate capacity at various current densities was found to be a value of 138.5  $\text{mAh g}^{-1}$ , mainly due to stable chemical structures and electrochemical properties (Fig. S10b). As shown in Fig. 6j,

from the additional measurements for comparison, the Nyquist plots with equivalent circuit (inset) for the  $\text{Co}(\text{OH})_2$ -RGOC,  $\text{Co}_3\text{O}_4$ -RGOC-250, and  $\text{Co}_3\text{O}_4$ -RGOC-350 indicated that the  $\text{Co}_3\text{O}_4$ -RGOC-250 has superior ion diffusion, lower electrochemical resistance ( $R_s$ ) of 0.38  $\Omega$ , and charge transfer resistance ( $R_{\text{ct}}$ ) of 0.45  $\Omega$  due to the double conductive networks (Fig. S11). As typical structures of “ion-buffering reservoirs,” Fig. 6k schematically illustrates the charge–discharge process of the  $\text{Co}_3\text{O}_4$ -RGOC composites in KOH electrolyte. The excellent cooperative contributions can be summarized as follows: (i) in the horizontal plane direction, the rGO nanosheets act as intermediate layer framework to form sandwich-like structures and further improve the electron transport; (ii) in the perpendicular direction, a series of CNTs can effectively prevent rGO nanosheets from restacking in the solvothermal synthesis process, meanwhile increase the electronic conductivity of the as-prepared composites; (iii) in the interior of sandwich-like  $\text{Co}_3\text{O}_4$ -rGO, the 2D transversal rGO nanosheets and 1D longitudinal CNTs can form double conductive networks to enhance the electrochemical properties of not only electron transport but also double-layer capacitance with synergistic effect; and (iv) on the exterior of hierarchical porous

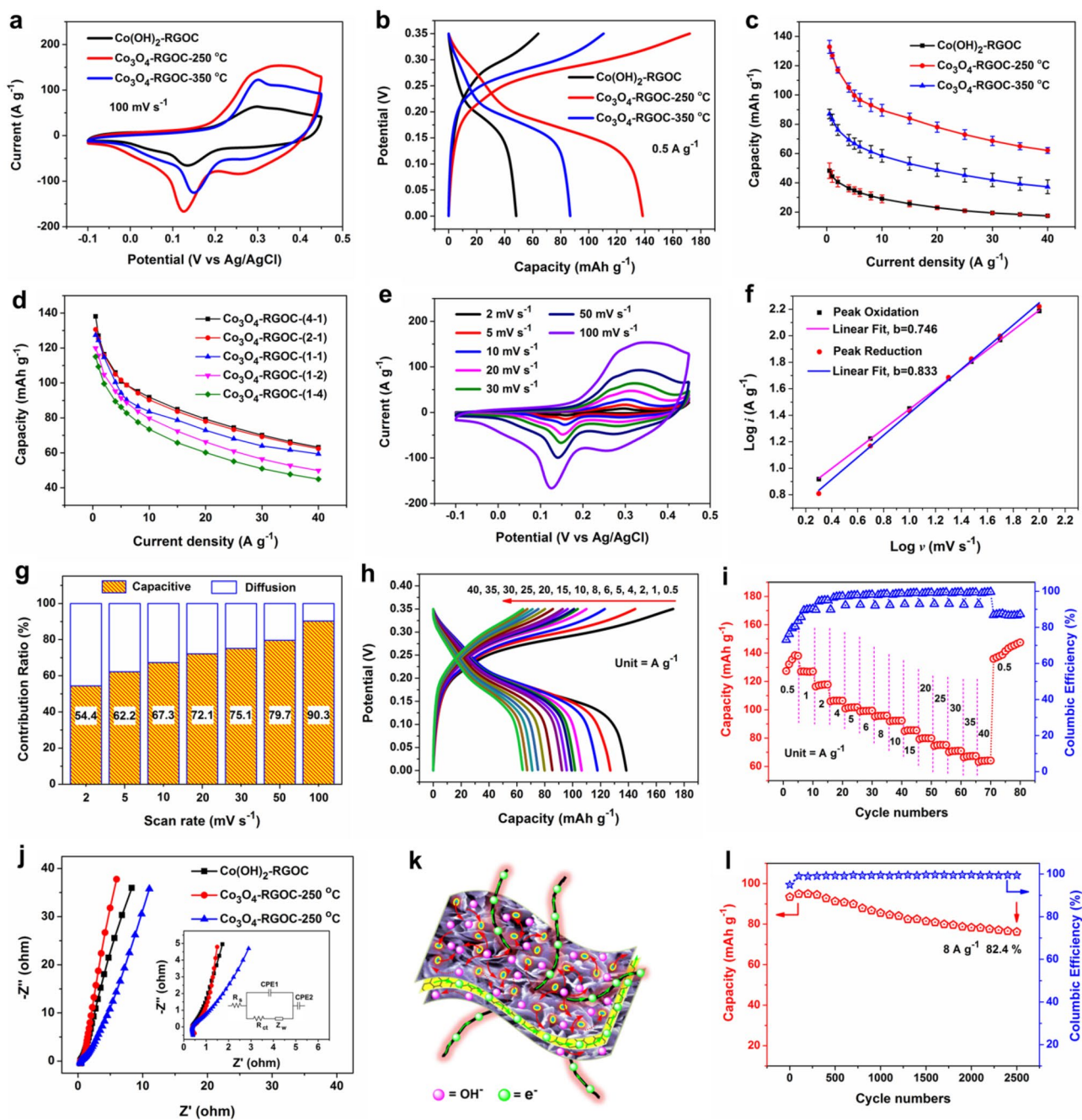


**Fig. 6** Electrochemical performance comparison of  $\text{Co(OH)}_2\text{-RGOC}$ ,  $\text{Co}_3\text{O}_4\text{-RGOC-250}$ , and  $\text{Co}_3\text{O}_4\text{-RGOC-350}$  (all these three kinds of electrode materials with rGO/CNTs mass ratio of 4:1): **a** CV curves at  $100 \text{ mV s}^{-1}$ , **b** GCD curves at  $0.5 \text{ A g}^{-1}$ , **c** The average (at least four samples) specific capacity at various current densities. **d** The specific capacity of  $\text{Co}_3\text{O}_4\text{-RGOC-250}$  with different rGO/CNTs mass ratio of 4:1, 2:1, 1:1, 1:2, and 1:4. The electrochemical prop-

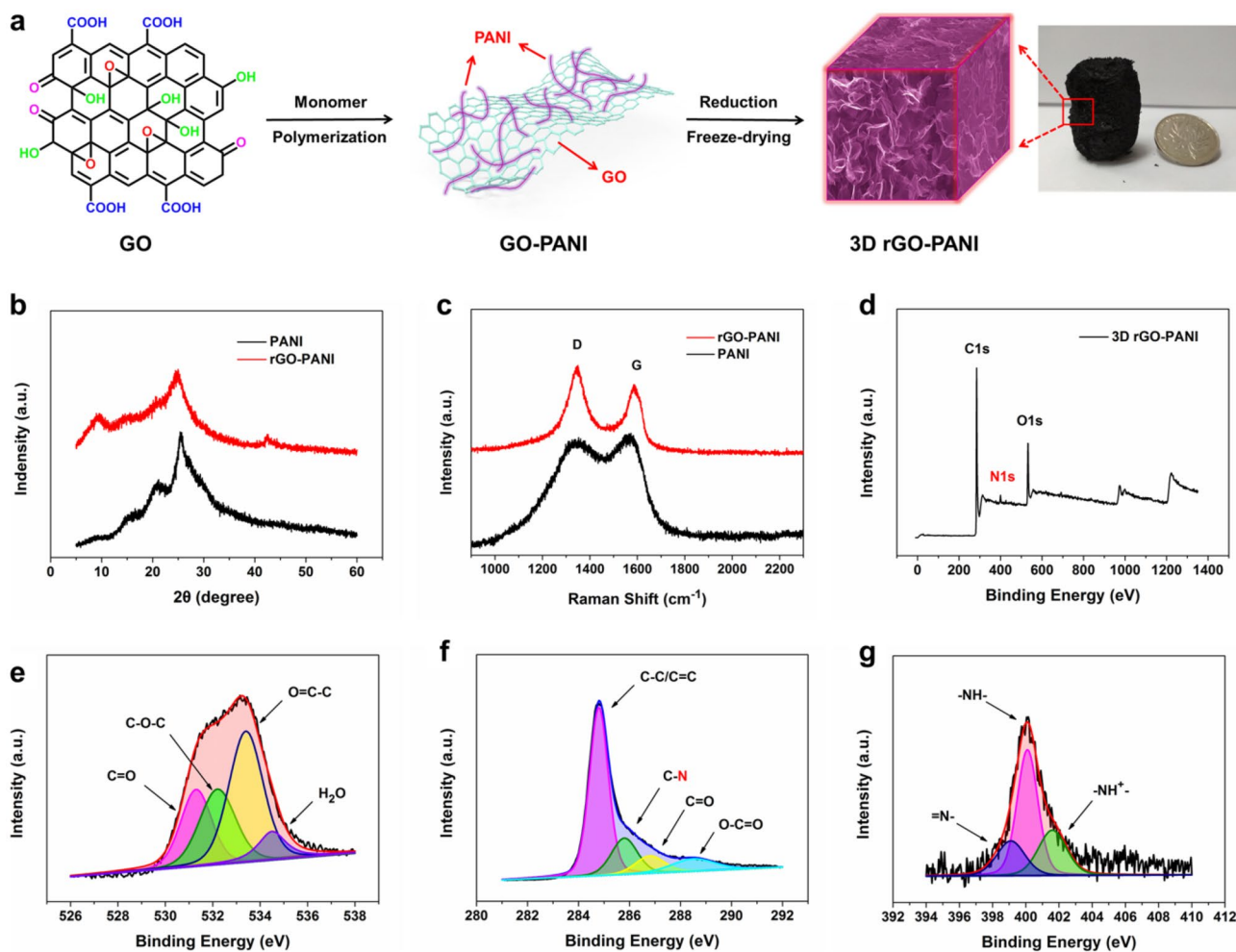
erties of the  $\text{Co}_3\text{O}_4\text{-RGOC}$  (sintering at  $250 \text{ }^\circ\text{C}$ , rGO/CNTs mass ratio of 4:1): **e** CV curves, **f**  $b$  value, **g** capacitive and diffusion-controlled ratio at various scan rates, **h** GCD curves, **i** rate performance, **j** Nyquist plots (inset equivalent circuit) of the  $\text{Co(OH)}_2\text{-RGOC}$ ,  $\text{Co}_3\text{O}_4\text{-RGOC-250}$ , and  $\text{Co}_3\text{O}_4\text{-RGOC-350}$  for comparison, **k** Schematic illustration of charge–discharge process, **l** Cycling performance

sandwich-like  $\text{Co}_3\text{O}_4\text{-rGO}$  composites, the electrolyte ions can fill in the opened honeycomb-like structures as “ion-buffering reservoirs” to ensure the sufficient reversible Faradaic redox reactions even at high current densities. Additionally, Fig. 6l describes the

good rate performance and excellent cycling performance at  $8 \text{ A g}^{-1}$ , indicating the capacitance retention of 82.4% after 2500 cycles with Coulombic efficiency of 99.4% for promising electrode materials.

Due to the superiority of the interconnected porous network structures, excellent electrical conductivity, and large specific surface area, GAs as negative EDLCs of the asymmetric supercapacitors have attracted tremendous attention. However, the GAs also suffers from restacking because of van der Waals and  $\pi$ - $\pi$  interactions. Consequently, to further improve the electron transport, hydrophilicity, and ion diffusion rate, the promising conductive polymer polyaniline (PANI) can be introduced into the 3D porous structures by in situ polymerization, as presented in the schematic preparation processes (Fig. 7a), in which the 3D rGO-PANI aerogels were prepared based on GO dispersion and aniline monomer and sequentially dealt by chemical reduction and freeze-drying process, respectively. In this structure, the PANI polymers may effectively prevent the restacking and agglomeration of rGO sheets during the reduction process. Besides, the in situ polymerized PANI polymers are clearly beneficial for the electrochemical properties to enhance the hydrophilicity and electronic conductivity by synergistic

effects, such as specific capacitance, high rate performance, and excellent cycling life. Compared with the pure PANI powders (the peak of  $25.5^\circ$ ), the XRD pattern exhibited a broad peak at  $24.8^\circ$  (with a lower  $2\theta$  angle) corresponding to the (002) plane of rGO-PANI as shown in Fig. 7b, confirming the components of 3D rGO-PANI aerogels. Meanwhile, the characteristic contrast at 1345 and  $1587\text{ cm}^{-1}$  can be attributed to the D- and G-band in the Raman spectra (Fig. 7c), respectively. Furthermore, the fully scanned XPS spectrum delivers the main elements of C, O, and N as presented in Fig. 7d. Moreover, the C/O ratio was calculated as 6.73:1, and the atomic ratio of N element was found to be 2.6% (Table S3), respectively. For the O 1s spectrum (Fig. 7e), four peaks can be indexed as the C=O (531.3 eV), O-C-O (532.2 eV), O=C-O (533.4 eV), and physically adsorbed water (534.5 eV), respectively. Furthermore, the abundant oxygen containing groups are beneficial for the hydrophilicity of aqueous electrolyte on the surface of the 3D rGO-PANI composites. The C 1s XPS spectrum in



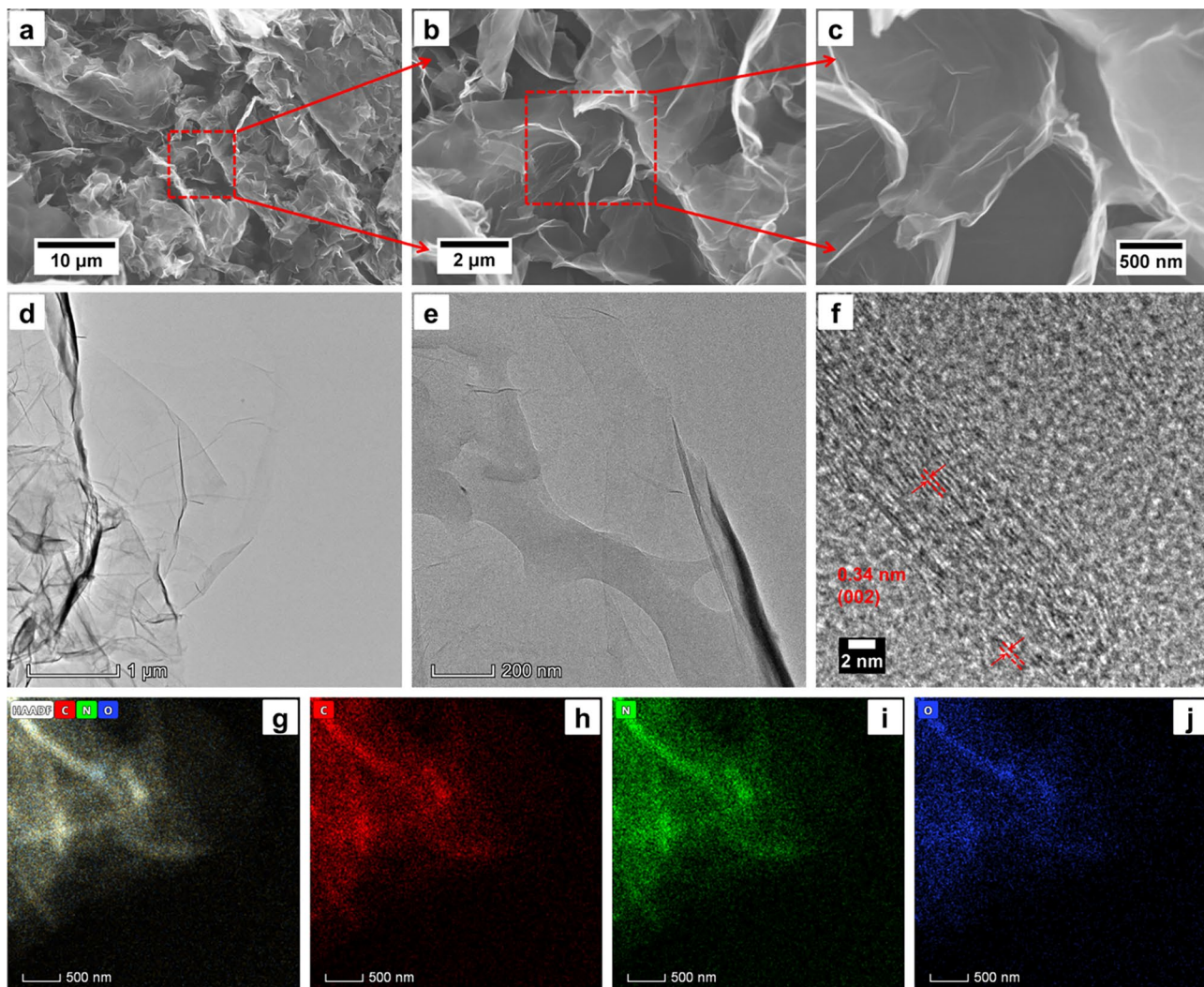
**Fig. 7** a Procedure for the preparation of 3D rGO-PANI aerogels (the inset shows the photograph). b–c XRD patterns, Raman spectra of PANI powders, and 3D rGO-PANI aerogels. d–g The fully scanned XPS spectrum, O 1s, C 1s, and N 1s XPS spectra of 3D rGO-PANI

Fig. 7f indicates C–C/C=C (284.8 eV), C=O (286.8 eV), O=C–O (288.5 eV), and especially C–N (285.8 eV) [57]. Subsequently, the N 1s XPS spectrum (Fig. 7g) assigned to 399.1 eV (=N–, di-imine nitrogen), 400.1 eV (–NH–, benzenoid diamine nitrogen), and 401.6 eV (–NH<sup>+</sup>–, nitrogen with a positive charge) [57, 58], respectively.

The surface morphology of 3D rGO-PANI aerogels was observed by the SEM and TEM measurements as shown in Fig. 8a–e. Notably, the interconnected porous network structures with opened honeycomb-like space appeared with the wrinkled graphene sheets as pore walls, which can be filled with the ample electrolyte ions based on typical “ion-buffering reservoirs” in the charge–discharge process to ensure the enhanced electrochemical performance, as demonstrated in Fig. S12. In Fig. 8f, the HRTEM image reveals the (002) planes of CNTs, thus corresponding to the 0.34 nm lattice spaces. Moreover, the C, N, and O

elements were evenly distributed in the rGO-PANI aerogel structures (Fig. 8g–j).

To deeply investigate the electrochemical performance, the CV tests were performed for 3D rGO-PANI aerogels, as presented in Fig. 9a. 3D rGO aerogels and pure PANI at 100 mV s<sup>−1</sup> were set for comparison in 6 M KOH aqueous electrolyte, in which the 3D rGO-PANI electrode materials displayed obviously larger CV area by the area integration according to the higher specific capacity. Notably, the nearly rectangular CV curve of 3D rGO aerogels exhibited ideal EDLC behaviors as shown in Fig. 9b. Meanwhile, the 3D rGO-PANI aerogels represent a larger area of CV curve with obvious redox peaks due to PANI polymers. Based on the Dunn methods [54], the calculated *b* values are 0.970 and 0.961 (closer to 1) as shown in Fig. 9c, demonstrating the capacitive process according to pseudocapacitive or EDLC. Furthermore, Fig. 9d represents the capacitive contribution



**Fig. 8** a–c Low- and high-magnification SEM images of 3D rGO-PANI aerogels. d–e Low- and high-magnification TEM images, f HRTEM image, g–j the EDS elemental mapping analysis of C-K, N-K, and O-K

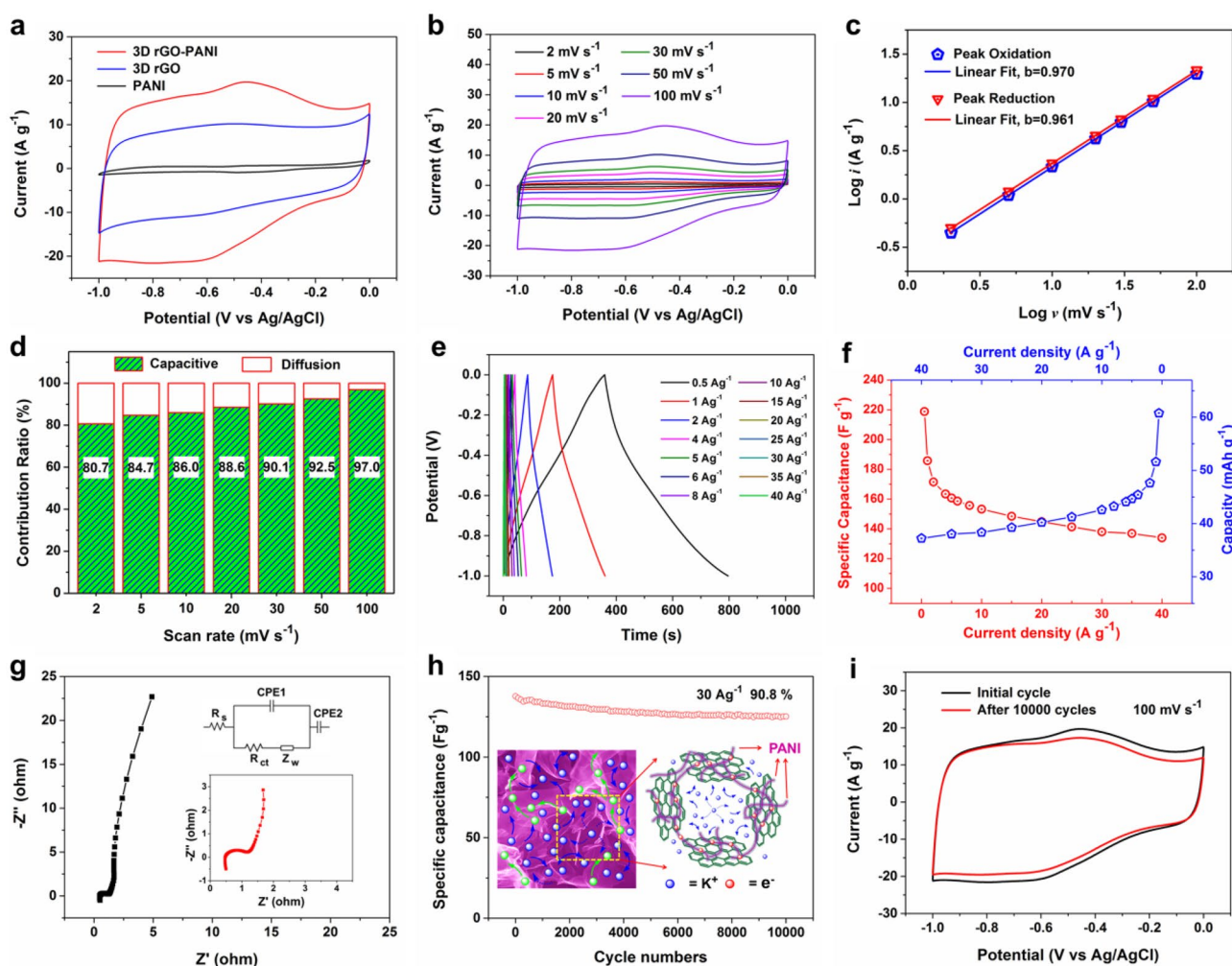


**Fig. 9** **a** The comparison of CV curves at  $100 \text{ mV s}^{-1}$  of 3D rGO-PANI aerogels, 3D rGO aerogels, and pure PANI. The electrochemical properties of 3D rGO-PANI aerogels: **b** CV curves at different scan rates, **c**  $b$  value, and **d** capacitive and diffusion-controlled ratio at various scan rates, **e** GCD curves, **f** the specific capacitance/capac-

ity at various current densities, **g** Nyquist plots (the inset shows the equivalent circuit), and **h** cycling performance at a current density of  $30 \text{ A g}^{-1}$ , and the inset shows schematic illustration for charge-discharge process in KOH solution. **i** CV curves of the initial cycle and after 10,000 cycles for comparison

ratio of 80.7%, 84.7%, 86.0%, 88.6%, 90.1%, 92.5%, and 97.0% from 2 to  $100 \text{ mV s}^{-1}$ , respectively. Figure 9e-f represents the GCD curves and specific capacitance/capacity, which describes high specific capacitance of  $218.8 \text{ F g}^{-1}$  (capacity of  $60.8 \text{ mAh g}^{-1}$ ) at  $0.5 \text{ A g}^{-1}$  and  $134.0 \text{ F g}^{-1}$  ( $37.2 \text{ mAh g}^{-1}$ ) at  $40 \text{ A g}^{-1}$  (with capacitance retention of 61.2%), respectively. Additionally, the Nyquist impedance spectra indicate  $R_s$  of  $0.48 \Omega$  and  $R_{ct}$  of  $0.85 \Omega$  as shown in Fig. 9g, corresponding to the reasonable electrical conductivity of graphene nanosheets and PANI polymers. Figure 9h represents the cycling performance of the 3D rGO-PANI at  $30 \text{ A g}^{-1}$ , and the specific capacitance only decreases 9.2% after 10,000 cycles, clearly indicating excellent chemical and structural stability. Accordingly, the CV curves of the initial cycle and after 10,000 charge-discharge cycles for comparison can keep nearly the same shapes and scan areas

(Fig. 9i), which further indicates a good agreement with the good cycling performance (Fig. S13). Impressively, the inset in Fig. 9h shows a schematic illustration of 3D rGO-PANI aerogel charge-discharge process in KOH solution. More importantly, 3D rGO-PANI aerogels exhibited the hierarchically interconnected porous structures with opened honeycomb-like space, which are composed of the randomly and crinkly oriented graphene nanosheets as “ion-buffering reservoirs.” In this intriguing structure, the electrolyte ions can freely be transported into the whole interspace of the interconnected porous structures from the external electrolyte with a shortened diffusion distance. Accordingly, the typically structured “ion-buffering reservoirs” can ensure excellent electrochemical properties, such as low contact resistance, good cycling performance, and high rate capacitance even at high current density.

As presented in Fig. 10a, the newly developed double ion-buffering reservoirs of  $\text{Co}_3\text{O}_4$ -RGOC//3D rGO-PANI ASCs were assembled with  $\text{Co}_3\text{O}_4$ -RGOC composites and 3D rGO-PANI aerogels. Figure 10b exhibits CV curves at different scan

rates with the combination of both electrical double-layer and battery-type capacitance, according to the electrochemical features of 3D rGO-PANI ( $-1.0-0$  V) and  $\text{Co}_3\text{O}_4$ -RGOC ( $-0.1-0.45$  V) at  $100 \text{ mV s}^{-1}$  for comparison (in separated

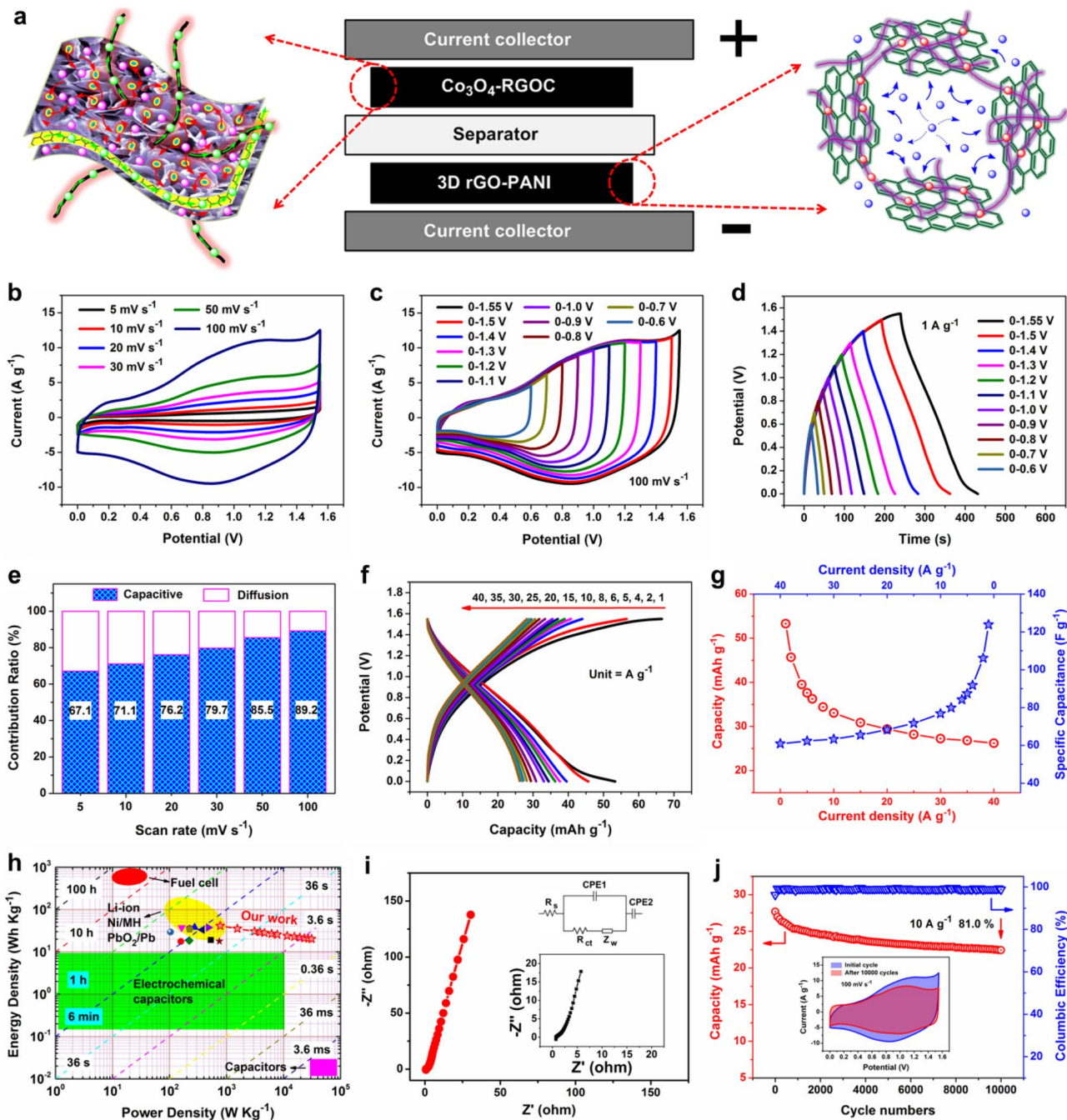


**Fig. 10** **a** Schematic illustration of the double ion-buffering reservoirs of asymmetric supercapacitors configuration  $\text{Co}_3\text{O}_4$ -RGOC//3D rGO-PANI. The electrochemical properties of  $\text{Co}_3\text{O}_4$ -RGOC//3D rGO-PANI: **b** CV curves at different scan rates. **c** CV curves measured at different potential windows (at  $100 \text{ mV s}^{-1}$ ). **d** GCD curves with the increase of the potential window (at  $1 \text{ A g}^{-1}$ ). **e** Capacitive and diffusion-controlled ratio at various scan rates. **f** GCD curves

at different current densities. **g** The specific capacity/capacitance at various current densities. **h** Ragone plots (compared with various energy storage devices and previously reported  $\text{Co}_3\text{O}_4$  asymmetric systems). **i** Nyquist plots of asymmetric supercapacitors devices (the inset shows the equivalent circuit). **j** Cycling performance at a current density of  $10 \text{ A g}^{-1}$ , the inset shows the comparison of CV curves (at  $100 \text{ mV s}^{-1}$ ) of the initial cycle and after 10,000 GCD cycles

potential windows, Fig. S14). From the combinatorial configuration of the  $\text{Co}_3\text{O}_4\text{-RGOC//3D rGO-PANI}$ , the optional voltage window is expected up to 1.55 V. As presented in Fig. 10c, a series of CV curves was collected from 0–0.6 to 0–1.55 V at  $100\text{ mV s}^{-1}$  in different potential windows, indicating that more redox reactions occurred for the larger current response with the operating potential window increasing to 1.55 V. Furthermore, Fig. 10d represents the GCD curves at  $1\text{ A g}^{-1}$  with the increase of the potential window in the range of 0–0.6 to 0–1.55 V, corresponding to the CV curves with different potential windows. Meanwhile, Fig. 10e shows the percentage contribution of the capacitive and diffusion contributions at various scan rates, indicating the capacitive contribution ratio of 67.1%, 71.1%, 76.2%, 79.7%, 85.5%, and 89.2% at 5, 10, 20, 30, 50, and  $100\text{ mV s}^{-1}$ , respectively. In addition, GCD curves of asymmetric supercapacitors device

were evaluated from 1 to  $40\text{ A g}^{-1}$  in Fig. 10f. Subsequently, the specific capacity/capacitance values were calculated at different current densities as exhibited in Fig. 10g. A relatively high rate performance was yielded as  $53.3\text{ mAh g}^{-1}$  at  $1\text{ A g}^{-1}$  (corresponding to the specific capacitance of  $123.8\text{ F g}^{-1}$ ) and  $26.2\text{ mAh g}^{-1}$  at  $40\text{ A g}^{-1}$  (corresponding to  $60.9\text{ F g}^{-1}$ ) with the capacitance retention of 49.2% (Fig. S15a–c), respectively. Accordingly, the Ragone plots were evidenced as  $41.3\text{ Wh kg}^{-1}$  at power densities of  $775\text{ W kg}^{-1}$  and  $20.3\text{ Wh kg}^{-1}$  at  $31,000\text{ W kg}^{-1}$  as represented in Fig. 10h. Compared to the previously reported energy storage devices and other  $\text{Co}_3\text{O}_4$  ASCs, the work represented higher energy density in the Ragone chart (Table S4), such as  $\text{Co}_3\text{O}_4\text{-GC//3D HRGC}$  ( $42.6\text{ Wh kg}^{-1}$ ,  $775\text{ W kg}^{-1}$ ) [13],  $\text{DBS-Co}_3\text{O}_4\text{//3D rGO}$  ( $25.5\text{ Wh kg}^{-1}$ ,  $400\text{ W kg}^{-1}$ ) [14],  $\text{Co}_3\text{O}_4\text{-G>N-PEGm//3D GCA}$  ( $34.4\text{ Wh kg}^{-1}$ ,  $400\text{ W kg}^{-1}$ ) [15],  $\text{Co}_3\text{O}_4\text{/NiO//AC}$  ( $35\text{ Wh}$

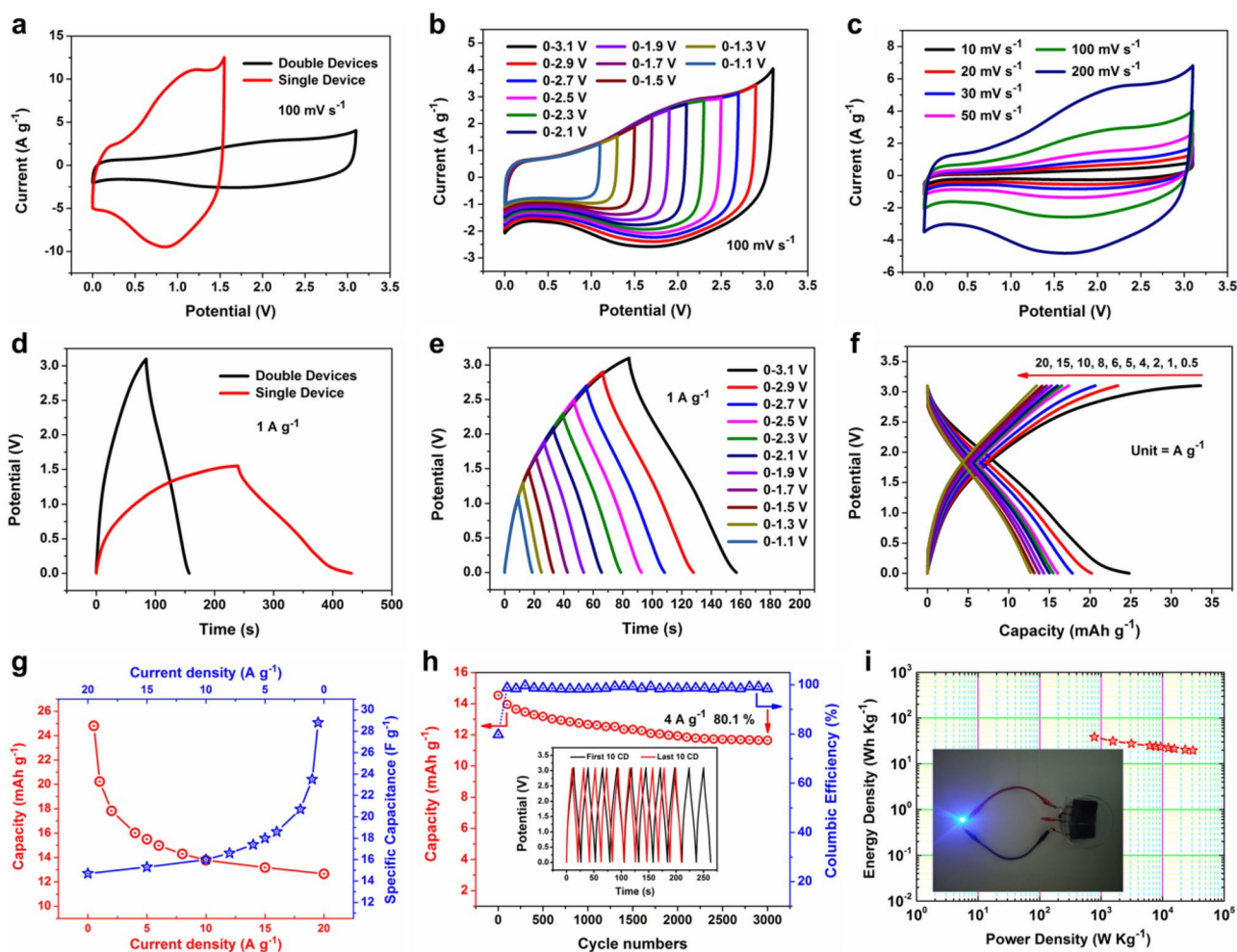


**Fig. 11** The electrochemical properties of the double devices  $\text{Co}_3\text{O}_4\text{-RGOC//3D rGO-PANI}$  connected in series: **a** CV curves of the single and the double devices for comparison. **b** CV curves at different potential windows (at  $100\text{ mV s}^{-1}$ ). **c** CV curves at different scan rates. **d** GCD curves of the single and the double devices for comparison. **e** GCD curves with the increase of the potential window

(at  $1\text{ A g}^{-1}$ ). **f** GCD curves at different current densities. **g** The specific capacity/capacitance at various current densities. **h** Cycling performance at a current density of  $4\text{ A g}^{-1}$ , the inset shows the initial 10 times GCD curves and that of the last 10 cycles. **i** Ragone plots, the inset shows the photograph of blue-light emitting diode (LED) lighted by the as-prepared double devices in series

$\text{kg}^{-1}$ ,  $540 \text{ W kg}^{-1}$ ) [21],  $\text{Co}_3\text{O}_4@\text{Co}_9\text{S}_8//\text{AC}$  ( $26.1 \text{ Wh kg}^{-1}$ ,  $871.6 \text{ W kg}^{-1}$ ) [23],  $\text{Co}_3\text{O}_4@\text{NiMn-LDHm/NF//AC}$  ( $38.4 \text{ Wh kg}^{-1}$ ,  $800 \text{ W kg}^{-1}$ ) [59],  $\text{Co}_3\text{O}_4@\text{CC//ACF}$  ( $26.6 \text{ Wh kg}^{-1}$ ,  $137 \text{ W kg}^{-1}$ ) [60],  $\text{Al}_2\text{O}_3/\text{Co}_3\text{O}_4/\text{G//AC}$  ( $40.1 \text{ Wh kg}^{-1}$ ,  $410.9 \text{ W kg}^{-1}$ ) [61],  $\text{rGO-Co}_3\text{O}_4/\text{NF//AC/NF}$  ( $20 \text{ Wh kg}^{-1}$ ,  $1200 \text{ W kg}^{-1}$ ) [62],  $\text{Co}_3\text{O}_4/\text{Fe}_2\text{O}_3//\text{Co}_3\text{O}_4/\text{Fe}_2\text{O}_3$  ( $35.15 \text{ Wh kg}^{-1}$ ,  $1125 \text{ W kg}^{-1}$ ) [63],  $\text{Co}_3\text{O}_4/\text{CoV}_x\text{O}_y//\text{AC}$  ( $26.1 \text{ Wh kg}^{-1}$ ,  $400 \text{ W kg}^{-1}$ ) [64],  $\text{Co}_3\text{O}_4/\text{NF//N-rGO/NF}$  ( $22.2 \text{ Wh kg}^{-1}$ ,  $800 \text{ W kg}^{-1}$ ) [65],  $\text{Co}_3\text{O}_4\text{-MXene}@/\text{NF//PANIC}@/\text{CFP}$  ( $26.06 \text{ Wh kg}^{-1}$ ,  $700 \text{ W kg}^{-1}$ ) [66], and  $\text{Co}_3\text{O}_4@\text{CoNiS//AC}$  ( $46.95 \text{ Wh kg}^{-1}$ ,  $400 \text{ W kg}^{-1}$ ) [67]. Furthermore, the  $R_s$  and  $R_{ct}$  of the as-assembled  $\text{Co}_3\text{O}_4\text{-RGOC//3D rGO-PANI}$  can be determined as  $0.72 \Omega$  and  $1.24 \Omega$  in the Nyquist plots (Fig. 10i), respectively. More importantly, the cycling performance of the asymmetric supercapacitor devices was determined in Fig. 10j, and the specific capacitance only decreased by 19.0% with high Coulombic efficiency of 99.5% at  $10 \text{ A g}^{-1}$  even after 10,000 cycles (Fig. S15d). Moreover, the CV curves of the initial cycle and after 10,000 charge–discharge cycles at  $100 \text{ mV s}^{-1}$  for comparison (inset Fig. 10j) exhibited excellent cycling performance.

To further demonstrate the electrochemical properties of  $\text{Co}_3\text{O}_4\text{-RGOC//3D rGO-PANI}$  asymmetric supercapacitors for practical applications, the double devices of  $\text{Co}_3\text{O}_4\text{-RGOC//3D rGO-PANI}$  were connected serially and systematically evaluated. Compared with the single device, the serially integrated devices exhibited similar shapes of CV at  $100 \text{ mV s}^{-1}$  (Fig. 11a) curves GCD curves at  $1 \text{ A g}^{-1}$  (Fig. 11d) with the increased potential window  $3.1 \text{ V}$ . Moreover, a series of CV curves (Fig. 11b) and GCD curves (Fig. 11e) in the increasing potential windows from  $0 - 1.1$  to  $0 - 3.1 \text{ V}$  have indicated a larger current response according to more redox reactions occurred in the electrochemical processes. Similarly, the doubled devices were evaluated by CV curves (Fig. 11c) at various scan rates from  $10$  to  $200 \text{ mV s}^{-1}$  and GCD curves (Fig. 11f) at discharge current densities range of  $0.5$  to  $20 \text{ A g}^{-1}$ , corresponding to the voltage plateaus versus the redox peaks compared with the electrochemical characteristics of the single device, respectively. Accordingly, the specific capacity of the double devices can be calculated as  $24.8 \text{ mAh g}^{-1}$  at  $0.5 \text{ A g}^{-1}$  based on the total mass of the active materials, corresponding to the capacitance of  $28.8 \text{ F g}^{-1}$  as shown in Fig. 11g. Moreover, Fig. 11h exhibits the cycling performance with 80.1% capacitance retention with high Coulombic efficiency of 98.6% at  $4 \text{ A g}^{-1}$  after 3000 cycles (worse than the single device) (Fig. S16). The inset displays the GCD curves for the initial 10 times and the last 10 cycles for comparison. Furthermore, the Ragone plots can estimate the energy density of  $38.5 \text{ Wh kg}^{-1}$  at power densities of  $775 \text{ W kg}^{-1}$  as exhibited in Fig. 11i, and the inset shows the photograph of blue-light LED ( $3.0 \text{ V}$ ,  $0.06 \text{ W}$ ) lit up by the series double devices for potential applications.

## 4 Conclusions

In summary, we developed the promising hierarchical porous sandwich-like  $\text{Co}_3\text{O}_4\text{-RGOC}$  ternary composites as typical battery-type positive electrode materials via a facile solvothermal method, in which a series of  $\text{Co}_3\text{O}_4$  nanosheets presented typical “ion-buffering reservoirs” opened porous honeycomb-like structures with filled electrolyte on the exterior, and the interpenetrating rGO (in the horizontal plane direction) and CNTs (in the perpendicular direction) can act as double conductive networks in the interior. In addition, the 3D rGO-PANI aerogels as negative electrode materials were also prepared by in situ polymerization to improve the surface area coverage, hydrophilicity, and electronic conductivity. Besides, the fabricated double ion-buffering reservoirs of  $\text{Co}_3\text{O}_4\text{-RGOC//3D rGO-PANI}$  asymmetric supercapacitors devices present high energy density of  $41.3 \text{ Wh kg}^{-1}$  at a power density of  $775 \text{ W kg}^{-1}$  with excellent electrochemical performance and ultra-long cycle performance for energy storage and conversion. Our present work provides an innovative strategy and new concepts to design the novel double ion-buffering reservoirs of asymmetric supercapacitors based on the metal oxides with opened honeycomb-like structures as positive electrode materials and the 3D graphene aerogels as negative electrode materials.

**Supplementary Information** The online version contains supplementary material available at <https://doi.org/10.1007/s42114-022-00532-0>.

**Funding** This work was supported by the Science and Technology Project of Henan Province (No. 222102240103 and 192102210048); the Natural Science Foundation of Henan Province (No. 212300410099); the Basic Science Research Program through the National Research Foundation of Korea (NRF) funded by the Ministry of Education (NRF-2020R111A3070962); the National Research Foundation (NRF) of Korea under the auspices of the Ministry of Science and ICT (NRF-2021R1A5A1032937); and the Ph. D. Research Start-up Fund of Anyang Institute of Technology (No. BJSJ2019033).

## Declarations

**Conflict of interest** The authors declare no competing interests.

## References

- Li GQ, Ji YS, Zuo DY, Xu J, Zhang HW (2019) Carbon electrodes with double conductive networks for high-performance electrical double-layer capacitors. *Adv Compos Hybrid Mater* 2:456–461
- Zhuang Z, Wang WJ, Wei YD, Li TX, Ma ML, Ma Y (2021) Preparation of polyaniline nanorods/manganese dioxide nanoflowers core/shell nanostructure and investigation of electrochemical performances. *Adv Compos Hybrid Mater* 4:938–945
- Zhao YL, Liu F, Zhu KJ, Maganti S, Zhao ZY, Bai PK (2022) Three-dimensional printing of the copper sulfate hybrid composites for supercapacitor electrodes with ultra-high areal and



- volumetric capacitances. *Adv Compos Hybrid Mater.* <https://doi.org/10.1007/s42114-022-00430-5>
4. Sun Z, Qu KQ, Li JH, Yang S, Yuan BN, Huang ZH, Guo ZH (2021) Self-template biomass-derived nitrogen and oxygen co-doped porous carbon for symmetrical supercapacitor and dye adsorption. *Adv Compos Hybrid Mater* 4:1413–1424
  5. Xu MM, Huang YQ, Chen RW, Huang QB, Yang Y, Zhong LX, Ren JL, Wang XH (2021) Green conversion of ganoderma lucidum residues to electrode materials for supercapacitors. *Adv Compos Hybrid Mater* 4:1270–1280
  6. Patil SS, Bhat TS, Teli AM, Beknalkar SA, Dhavale SB, Faras MM, Karanjkar MM, Patil PS (2020) Hybrid solid state supercapacitors (HSSC's) for high energy & power density: an overview. *Eng Sci* 12:38–51
  7. Wang YZ, Liu YX, Wang C, Liu H, Zhang JX, Lin J, Fan JC, Ding T, Ryu JE, Guo ZH (2020) Significantly enhanced ultrathin NiCo-based MOF nanosheet electrodes hybridized with  $Ti_3C_2T_x$  MXene for high performance asymmetric supercapacitor. *Eng Sci* 9:50–59
  8. Hou CX, Wang MV, Vupputuri S, Chao YF, Guo ZH, Wang CY, Du W (2020) Recent advances in  $Co_3O_4$  as anode materials for high-performance lithium-ion batteries. *Eng Sci* 11:19–30
  9. Hou CX, Yang WY, Xie XB, Sun XQ, Wang J, Naik N, Pan D, Mai XM, Guo ZH, Dang F, Du W (2021) Agaric-like anodes of porous carbon decorated with  $MoO_2$  nanoparticles for stable ultralong cycling lifespan and high-rate lithium/sodium storage. *J Colloid Interface Sci* 596:396–407
  10. Li SH, Yang CY, Sarwar S, Nautiyal A, Zhang PF, Du HS, Liu N, Yin JL, Deng KL, Zhang XY (2019) Facile synthesis of nanostructured polyaniline in ionic liquids for high solubility and enhanced electrochemical properties. *Adv Compos Hybrid Mater* 2:279–288
  11. Zhai YJ, Yang WY, Xie XB, Sun XQ, Wang J, Yang XY, Naik N, Kimura H, Du W, Guo ZH, Hou CX (2022)  $Co_3O_4$  nanoparticles dotted hierarchical-assembled carbon nanosheet frameworks catalysts with formation/decomposition mechanisms of  $Li_2O_2$  for smart lithium-oxygen batteries. *Inorg Chem Front* 9:1115–1124
  12. Ling W, Wang PP, Chen Z, Wang H, Wang JQ, Ji ZY, Fei JB, Ma ZY, He N, Huang Y (2020) Nanostructure design strategies for aqueous zinc-ion batteries. *ChemElectroChem* 7:2957–2978
  13. Lai CW, Wang SH, Cheng LL, Wang YX, Fu L, Sun Y, Lin BP (2021) High-performance asymmetric supercapacitors of advanced double ion-buffering reservoirs based on battery-type hierarchical flower-like  $Co_3O_4$ -GC microspheres and 3D holey graphene aerogels. *Electrochim Acta* 365
  14. Lai CW, Sun Y, Zhang XQ, Yang H, Kang WW, Lin BP (2018) Advanced flower-like  $Co_3O_4$  with ultrathin nanosheets and 3D rGO aerogels as double ion-buffering reservoirs for asymmetric supercapacitors. *Electrochim Acta* 271:379–387
  15. Lai CW, Sun Y, Zhang XQ, Yang H, Lin BP (2018) High-performance double ion-buffering reservoirs of asymmetric supercapacitors based on flower-like  $Co_3O_4$ -G>N-PEGm microspheres and 3D rGO-CNT>N-PEGm aerogels. *Nanoscale* 10:17293–17303
  16. Lai CW, Qu XX, Zhao HH, Hong SW, Lee K (2022) Improved performance in asymmetric supercapacitors utilized by dual ion-buffering reservoirs based on honeycomb-structured  $NiCo_2O_4$  and 3D rGOPPy aerogels. *Appl Surface Sci* 586
  17. Lai CW, Lee K (2022) Double ion-buffering reservoirs of advanced  $NiCo/G$ -PANI asymmetric supercapacitors with high performance. *J Alloys Compd* 907
  18. Lai CW, Sun Y, Zhang XQ, Yang H, Lin BP (2018) Gradual “OH<sup>-</sup>-incursion” outside-inside strategy in construction of 3D flower-like  $Co_3O_4$ -CNT>N-PEGm hierarchical microspheres for supercapacitors. *Mater Today Energy* 9:27–38
  19. Lai CW, Sun Y, Lin BP (2019) Synthesis of sandwich-like porous nanostructure of  $Co_3O_4$ -rGO for flexible all-solid-state high-performance asymmetric supercapacitors. *Mater Today Energy* 9:342–352
  20. Wang DW, Li F, Liu M, Lu GQ, Cheng HM (2009) 3D aperiodic hierarchical porous graphitic carbon material for high-rate electrochemical capacitive energy storage. *Angew. Chem. Inter Ed* 48:1525–1525
  21. Wei HL, Guo XW, Wang Y, Zhou ZY, Lv HF, Zhao Y, Gu ZJ, Chen ZX (2022) Inherently porous  $Co_3O_4$ @NiO core-shell hierarchical material for excellent electrochemical performance of supercapacitors. *Appl Surface Sci* 574
  22. Cao JM, Li JZ, Zhou L, Xi YL, Cao X, Zhang YM, Han W (2021) Tunable agglomeration of  $Co_3O_4$  nanowires as the growing core for in situ formation of  $Co_2NiO_4$  assembled with polyaniline-derived carbonaceous fibers as the high-performance asymmetric supercapacitors. *J Alloys Compd* 853
  23. Lian XJ, Guo W, Wu YL, Tian YM, Wang S (2021) The structure-stabilized  $Co_3O_4$ @ $Co_9S_8$  core-shell nanorods synthesized by in-situ sulfuration of  $Co_3O_4$  for high-performance supercapacitors. *J Alloys Compd* 865
  24. Tian YR, Yang X, Nautiyal A, Zheng YY, Guo QP, Luo JJ, Zhang XY (2019) One-step microwave synthesis of  $MoS_2/MoO_3$ @graphite nanocomposite as an excellent electrode material for supercapacitors. *Adv Compos Hybrid Mater* 2:151–161
  25. Lai CW, Wang YX, Fu L, Song HX, Liu B, Pan D, Guo ZH, Seok I, Li KW, Zhang HR, Dong MY (2022) Aqueous flexible all-solid-state NiCo-Zn batteries with high capacity based on advanced ion-buffering reservoirs of  $NiCo_2O_4$ . *Adv Compos Hybrid Mater* 5:536–546
  26. Ma YP, Xie XB, Yang WY, Yu ZP, Sun XQ, Zhang YP, Yang XY, Kimura H, Hou CX, Guo ZH, Du W (2021) Recent advances in transition metal oxides with different dimensions as electrodes for high-performance supercapacitors. *Adv Compos Hybrid Mater* 4:906–924
  27. Lai CW, Cheng LL, Sun Y, Lee K, Lin BP (2021) Alkaline aqueous rechargeable Ni-Fe batteries with high-performance based on flower-like hierarchical  $NiCo_2O_4$  microspheres and vines-grapes-like  $Fe_3O_4$ -NGC composites. *Appl Surface Sci* 563
  28. Qu XX, Liu YH, Li BB, Xing BL, Huang GX, Zhang CX, Hong SW, Yu JL, Cao YJ (2020) Synthesis of high reversibility anode composite materials using T- $Nb_2O_5$  and coal-based graphite for lithium-ion battery applications. *Energy Fuels* 34:3887–3894
  29. Liu S, Du HS, Liu K, Ma MG, Kwon YE, Si CL, Ji XX, Choi SE, Zhang XY (2021) Flexible and porous  $Co_3O_4$  carbon nanofibers as binder free electrodes for supercapacitors. *Adv Compos Hybrid Mater* 4:1367–1383
  30. Qu KQ, Sun Z, Shi C, Wang WC, Xiao LD, Tian JY, Huang ZH, Guo ZH (2021) Dual-acting cellulose nanocomposites filled with carbon nanotubes and zeolitic imidazolate framework-67 (ZIF-67)-derived polyhedral porous  $Co_3O_4$  for symmetric supercapacitors. *Adv Compos Hybrid Mater* 4:670–683
  31. Xiao LD, Qi HJ, Qu KQ, Shi C, Cheng Y, Sun Z, Yuan BN, Huang ZH, Pan D, Guo ZH (2021) Layer-by-layer assembled free-standing and flexible nanocellulose/porous  $Co_3O_4$  polyhedron hybrid film as supercapacitor electrodes. *Adv Compos Hybrid Mater* 4:306–316
  32. Kang M, Zhou H, Wen PS, Zhao N (2021) Highly hierarchical porous ultrathin  $Co_3O_4$  nanosheets@Ni foam for high-performance supercapacitors. *ACS Appl Energy Mater* 4:1619–1627
  33. Yang F, Zhang K, Cen Z, Xu KB (2021) Rational construction of multidimensional oxygen-deficient  $Co_3O_4$  nanosheet/nanowire arrays as high-performance electrodes for aqueous Zn-ion batteries and asymmetric supercapacitors. *J Alloys Compd* 879
  34. Sun JF, Mu Q, Kimura H, Murugadoss V, He MX, Du W, Hou CX (2022) Oxidative degradation of phenols and substituted phenols in the water and atmosphere: A Review *Adv Compos Hybrid Mater.* <https://doi.org/10.1007/s42114-022-00435-0>
  35. Wu NN, Du WJ, Hu Q, Vupputuri S, Jiang QL (2021) Recent development in fabrication of Co nanostructures and their

- carbon nanocomposites for electromagnetic wave absorption. *Eng Sci* 13:11–23
36. Hong H, Gao L, Zheng YW, Xing XL, Sun F, Liu TX, Murugadoss V, Guo ZH, Yang M, Zhang H (2021) A path of multi-energy hybrids of concentrating solar energy and carbon fuels for low CO<sub>2</sub> emission. *ES Energy Environ* 13:1–7
  37. Guo BB, Liang GJ, Yu SX, Wang Y, Zhi CY, Bai JM (2021) 3D printing of reduced graphene oxide aerogels for energy storage devices: a paradigm from materials and technologies to applications. *Energy Storage Mater* 39:146–165
  38. Zou YB, Chen ZY, Peng ZY, Yu CY, Zhong WB (2021) Mechanically strong multifunctional three dimensional crosslinked aramid nanofiber/reduced holey graphene oxide and aramid nanofiber/ reduced holey graphene oxide/polyaniline hydrogels and derived films. *Nanoscale* 13:16734–16747
  39. Kumari S, Verma E, Kumar R, Upreti D, Prakash B, Maruyama T, Bagchi V (2021) Micropores within N, S co-doped mesoporous 3D graphene-aerogel enhance the supercapacitive performance. *New J Chem* 45:7523–7532
  40. Qu XX, Kang WW, Lai CW, Zhang CX, Hong SW (2022) A simple route to produce highly efficient porous carbons recycled from tea waste for high-performance symmetric supercapacitor electrodes. *Molecules* 27:791
  41. Li J, Sun Y, Kang WW, Wang PN, Zhang HJ, Zhang XQ, Yang H, Lin BP (2021) Green synthesis of cellulose/graphene oxide/ZIF8 derived highly conductivity integrated film electrode for supercapacitor. *Carbon* 185:599–607
  42. Liu QQ, Zhang LL, Chen HX, Jin JZ, Wang NY, Wang Y, Sui DP (2021) Sulfur and nitrogen co-doped three-dimensional graphene aerogels for high-performance supercapacitors: a head to head vertical bicyclic molecule both as pillaring agent and dopant. *Appl Surface Sci* 565
  43. Kung CY, Wang TL, Lin HY, Yang CH (2021) A high-performance covalently bonded self-doped polyaniline-graphene assembly film with superior stability for supercapacitors. *J Power Sources* 490
  44. Song P, He XM, Tao J, Shen XP, Yan ZY, Ji ZY, Yuan AH, Zhu GX, Kong LR (2021) H<sub>2</sub>SO<sub>4</sub>-assisted tandem carbonization synthesis of PANI@carbon@textile flexible electrode for high-performance wearable energy storage. *Appl Surface Sci* 535
  45. Liu ZH, Zhao ZY, Xu AZ, Li W, Qin YJ (2021) Facile preparation of graphene/polyaniline composite hydrogel film by electrodeposition for binder-free all-solid-state supercapacitor. *J Alloys Compd* 875
  46. Lai CW (2019) Construction of atomically ultrathin 3D flower-like α-Co(OH)<sub>2</sub> hierarchical microspheres with gradually “OH-incursion” outside inside strategy. *J Alloys Compd* 777:492–498
  47. Wang RH, Xu CH, Sun J, Liu YQ, Gao L, Lin CC (2013) Free-standing and binder-free lithium-ion electrodes based on robust layered assembly of graphene and Co<sub>3</sub>O<sub>4</sub> nanosheets. *Nanoscale* 5:6960–6967
  48. Hadjiev VG, Iliiev MN, Vergilov IV (1988) The Raman spectra of Co<sub>3</sub>O<sub>4</sub>. *J Phys C: Solid State Phys* 21:L199–L201
  49. Feng C, Zhang J, He Y, Zhong C, Hu W, Liu L, Deng Y (2015) Sub-3 nm Co<sub>3</sub>O<sub>4</sub> nanofilms with enhanced supercapacitor properties. *ACS Nano* 9:1730–1739
  50. Yin YD, Rioux RM, Erdonmez CK, Hughes S, Somorjai GA, Alivisatos AP (2004) Formation of hollow nanocrystals through the nanoscale Kirkendall effect. *Science* 304:711–714
  51. Fan HJ, Knez M, Scholz R, Hesse D, Nielsch K, Zacharias M, Gosele U (2007) Influence of surface diffusion on the formation of hollow nanostructures induced by the Kirkendall effect: the basic concept. *Nano Lett* 7:993–997
  52. Wu NN, Zhao BB, Liu JY, Li YL, Chen YB, Chen L, Wang M, Guo ZH (2021) MOF-derived porous hollow Ni/C composites with optimized impedance matching as lightweight microwave absorption materials. *Adv Compos Hybrid Mater* 4:707–715
  53. Wang JJ, Xiao GY, Zhang TQ, Hao S, Jia ZQ, Li YL (2021) Fabrication of Co<sub>3</sub>O<sub>4</sub>/polyaniline-based carbon electrode for high-performance supercapacitor. *J Alloys Compd* 863
  54. Kim HS, Cook JB, Lin H, Ko JS, Tolbert SH, Ozolins V, Dunn B (2017) Oxygen vacancies enhance pseudocapacitive charge storage properties of MoO<sub>3-x</sub>. *Nat Mater* 16:454–460
  55. Hou LR, Shi YY, Zhu SQ, Rehan M, Pang G, Zhang XG, Yuan CZ (2017) Hollow mesoporous hetero-NiCo<sub>2</sub>S<sub>4</sub>/Co<sub>9</sub>S<sub>8</sub> submicrospindles: unusual formation and excellent pseudocapacitance towards hybrid supercapacitors. *J Mater Chem A* 5:133–144
  56. Zhang HY, Wang JC, Sun Y, Zhang XQ, Yang H, Lin BP (2021) Wire spherical-shaped Co-MOF electrode materials for high-performance all-solid-state flexible asymmetric supercapacitor device. *J Alloys Compd* 879
  57. Yu HT, Ge X, Bulin CK, Xing RG, Li RH, Xin GX, Zhang BW (2017) Facile fabrication and energy storage analysis of graphene/PANI paper electrodes for supercapacitor application. *Electrochim Acta* 253:239–247
  58. Jeyaranjan A, Sakthivel TS, Neal CJ, Seal S (2019) Scalable ternary hierarchical microspheres composed of PANI/rGO/CeO<sub>2</sub> for high performance supercapacitor applications. *Carbon* 151:192–202
  59. Quan W, Xu YY, Wang YT, Meng SC, Jiang DL, Chen M (2019) Hierarchically structured Co<sub>3</sub>O<sub>4</sub>@glucose-modified LDH architectures for high-performance supercapacitors. *Appl Surface Science* 488:639–647
  60. Tao YJ, Wu YT, Chen H, Chen WJ, Wang JJ, Tong YF, Pei G, Shen ZH, Guan C (2020) Synthesis of amorphous hydroxyl-rich Co<sub>3</sub>O<sub>4</sub> for flexible high-rate supercapacitor. *Chem Eng J* 396
  61. Zhang GF, Qin P, Song JM (2019) Facile fabrication of Al<sub>2</sub>O<sub>3</sub>-doped Co<sub>3</sub>O<sub>4</sub>/graphene nanocomposites for high performance asymmetric supercapacitors. *Appl Surface Science* 493:55–62
  62. Raj S, Srivastava SK, Kar P, Roy P (2019) In situ growth of Co<sub>3</sub>O<sub>4</sub> nanoflakes on reduced graphene oxide-wrapped Ni-foam as high performance asymmetric supercapacitor. *Electrochim Acta* 302:327–337
  63. Wei XJ, Li YH, Peng HR, Gao D, Ou YQ, Yang YB, Hu JR, Zhang YH, Xiao P (2019) A novel functional material of Co<sub>3</sub>O<sub>4</sub>/Fe<sub>2</sub>O<sub>3</sub> nanocubes derived from a MOF precursor for high-performance electrochemical energy storage and conversion application. *Chem Eng J* 355:336–340
  64. Lv X, Huang WX, Tang JB, Tang L, Shi QW (2021) Synthesis of Co<sub>3</sub>O<sub>4</sub>/CoV<sub>x</sub>O<sub>y</sub> core-shell nanosheets arrays with interweaved nanowires as cathode materials for asymmetric supercapacitors. *Electrochim Acta* 380
  65. Wei G, Yan LQ, Huang HF, Yan FX, Liang XQ, Xu SK, Lan ZQ, Zhou WZ, Jin G (2021) The hetero-structured nanoarray construction of Co<sub>3</sub>O<sub>4</sub> nanowires anchored on nanoflakes as a high-performance electrode for supercapacitors. *Appl Surface Sci* 538
  66. Zhang YM, Cao JM, Yuan ZY, Zhao LJ, Wang LL, Han W (2021) Assembling Co<sub>3</sub>O<sub>4</sub> nanoparticles into MXene with enhanced electrochemical performance for advanced asymmetric supercapacitors. *J Colloid Interface Sci* 599:109–118
  67. Yan YQ, Ding SX, Zhou XY, Hu Q, Feng Y, Zheng QJ, Lin DM, Wei XJ (2021) Controllable preparation of core-shell Co<sub>3</sub>O<sub>4</sub>@CoNiS nanowires for ultra-long life asymmetric supercapacitors. *J Alloys Compd* 867

**Publisher's Note** Springer Nature remains neutral with regard to jurisdictional claims in published maps and institutional affiliations.